Surface-based and solid shell formulations of the 7-parameter shell model for layered CFRP and functionally graded power-based composite structures

J. Reinoso*[a], M. Paggi[b], P. Areias[c], A. Blázquez[a]

[a] *Elasticity and Strength of Materials Group, School of Engineering, Universidad de Sevilla, Camino de los Descubrimientos s/n, 41092, Seville, Spain* [b] *IMT School for Advanced Studies Lucca, Piazza San Francesco, 55100 Lucca, Italy* [c] *Department of Physics, University of Évora, Colégio Luís António Verney, Rua Romão Ramalho, 59, 7002-554 Évora, Portugal*

* Corresponding Author: jreinoso@us.es

Elasticity and Strength of Materials Group, School of Engineering, Universidad de Sevilla,
Camino de los Descubrimientos s/n, 41092, Seville, Spain

Surface-based and solid shell formulations of the 7-parameter shell model for layered CFRP and functionally graded power-based composite structures

Abstract

In this study, we present the extension of the so-called 7-parameter shell formulation to layered CFRP and functionally graded power-based composite structures using two different parametrizations: (i) the three-dimensional shell formulation, and (ii) the solid shell approach. Both numerical strategies incorporate the use of the Enhanced Assumed Strain (EAS) and the Assumed Natural Strain (ANS) methods to alleviate locking pathologies and are implemented into the FE code ABAQUS. The applicability of the current developments is demonstrated by means of several benchmark examples, whose results are compared with reference solutions using shell elements of ABAQUS, exhibiting an excellent level of accuracy

Keywords: Shells; Composite materials; Finite element method; Functionally graded materials

1 Introduction

In the last decades, an increasing interest in the incorporation of advanced composite materials in engineering structures has been devised. This trend arises from the need of producing components with an optimized behavior especially within the aerospace and automotive sectors. In general, composites offer several attractive advantages over traditional metallic materials and alloys due to their exceptional stiffness-weight and strength-weight ratios.

As a consequence of these demands, the profound knowledge related to the structural performance of shell-based composite structures has motivated the development of a large number of novel structural models and their corresponding numerical implementations. Formulations relying on the classical Kirchhoff-Love (known as 3-parameter model) and the Reissner-Mindlin (5-p model) concepts have been extensively employed in order to predict the mechanical performance of isotropic and composite shells undergoing small strains. However, the inextensibility of the shell director vector in both theories can lead to inaccurate results as well as the preclusion of the use of unmodified three-dimensional material models.

The previous limitations can be circumvented by means of refined theories, especially for laminated and functionally graded composite shells. Within this context, Carrera proposed the so-called Unified Formulation (CUF) [1, 2, 3], which introduced a basic kernel together with a series of thickness functions (using either series expansion or interpolation polynomials, among others) in order to generate different structural models, covering both *equivalent single layer* (ESL) and *Layer-Wise* (LW) approaches, see e.g. [4, 5, 6, 7, 8, 9, 10]. The compact representation of the CUF allows the achievement of a higher numerical accuracy through increasing the order of the underlying theoretical model. The potential of such modeling framework has been comprehensively proven by its application to coupled problems [11], and vibration analysis [12], among others.

Alternatively to CUF technique, shell formulations based on exact geometry concepts have been exploited in the last few years [13, 14, 15, 16]. This approach be interpreted as a step back into the 3-D continuum, as is envisaged in the fundamental works of Ericksen and Truesdell [17] and Nagdhi [18]. Complying with this approximation, usually denominated as *continuum-based degenerated shell elements*, the displacement and the position vector of the shell body (in the reference and current configurations) can be expressed as an infinite sum of functions of the in-plane coordinates $M(\xi^1, \xi^2) \subset \mathbb{R}^2$, which are multiplied by a series of terms which are expanded over the thickness direction $F(\xi^3) \subset \mathbb{R}$, whereby ξ^1, ξ^2 denote the in-plane curvilinear coordinates and ξ^3 identifies the out-of-plane coordinate. The truncation of such expansion up to the linear [19], quadratic [20] and cubic [21] terms in ξ^3 leads to the development of the so-called 6-p, 7-p and 12-p models, respectively.

In particular, since low-order interpolations are generally recommended for computationally efficient nonlinear applications, a special attention has been paid to the development of locking-free finite elements relying on the 6-p formulation. However, this shell model suffers from severe locking pathologies, which has been remedied through different numerical techniques in combination with the Assumed Natural Strain (ANS) [22, 23] method: (*i*) the Enhanced Assumed Strain (EAS) method [24, 25, 26, 27], (*ii*) the development of hybrid element formulations [28, 29, 30, 31, 32], and (*iii*) the use of the Reduced Integration (RI) [33, 34] techniques, among many other computational procedures.

Recalling Bischoff and Ramm, the 7-p shell model offers a good trade-off between numerical efficiency (using first-order elements) and accuracy for complex nonlinear simulations, see [15, 19, 35, 36, 37]. This formulation has been successfully extended to composite structures in [38, 39] and combined with fracture and damage methods in [40, 41, 42, 43]. Nevertheless, as discussed in [44], the 7-p model allows two different parametrization of the shell geometry to be considered: (*i*) three-dimensional shell elements (surface-based FE meshes), which consider a reference surface of the shell [20, 45, 16], and (*ii*) solid shell elements (solid-based FE meshes) that employs the position vectors of two points of the top and bottom surfaces of the body to define the shell kinematic field.

This paper addresses the extension of the 7-p shell model to composite laminated and functionally graded shell structures exploiting both parametrizations mentioned above, paying special attention to specific aspects regarding the implementation into finite element routines and the corresponding numerical performance. In line with [38, 39], locking pathologies are alleviated through the combined use of the EAS and ANS methods.

The rest of the manuscript is organized as follows. The fundamental concepts and notation of the current shell models are introduced in Sect.2. The fundamental of the EAS method and the constitutive formulations herewith developed for composites are presented in Sect.3, whereas Sect.4 addresses the numerical assessment of the current derivations. Finally, the main conclusions of this investigation are summarized in Sect.5.

2 Shell formulation: 7-parameter model

In this section, we briefly discuss the basic aspects of the 7-p model under consideration for the simulation of thin-walled composite structures. As mentioned above, two different kinematic parametrization are comprehensively analyzed: (*i*) the three-dimensional shell model (surface-based FE meshes) [15, 19], which is presented in Sect. 2.2, and (*ii*) the solid shell model [46], whose fundamental aspects are given in Sect. 2.3. The current derivations are presented within the context of the nonlinear Continuum Mechanics setting in order to provide a general modeling framework.

2.1 Basic notation

Consider an arbitrary shell body whose reference placement is identified by $\mathcal{B}_0 \in \mathbb{R}^3$. This shell experiences a macroscopic motion within a time interval $[0, t]$, which is denoted as $\boldsymbol{\varphi}(\mathbf{X}, t) : \mathcal{B}_0 \times [0, t] \to \mathbb{R}^3$, mapping the reference material points ($\mathbf{X}(\boldsymbol{\xi}) \in \mathcal{B}_0$) onto the current material points ($\mathbf{x}(\boldsymbol{\xi}) \in \mathcal{B}_t$), such that $\mathbf{x} = \boldsymbol{\varphi}(\mathbf{X}, t)$, see Fig. 1. The reference and current position vectors are functions of the material coordinates $\boldsymbol{\xi} = \{\xi^1, \xi^2, \xi^3\}$, which denote the parametric curvilinear coordinates $\xi^i \in [-1, 1]$ with $i = 1, 2, 3$. These coordinates are introduced in order to adequately describe the geometry and kinematics of curved structures. With the previous definitions at hand, the displacement field accordingly reads: $\mathbf{u}(\boldsymbol{\xi}) := \mathbf{x}(\boldsymbol{\xi}) - \mathbf{X}(\boldsymbol{\xi})$.

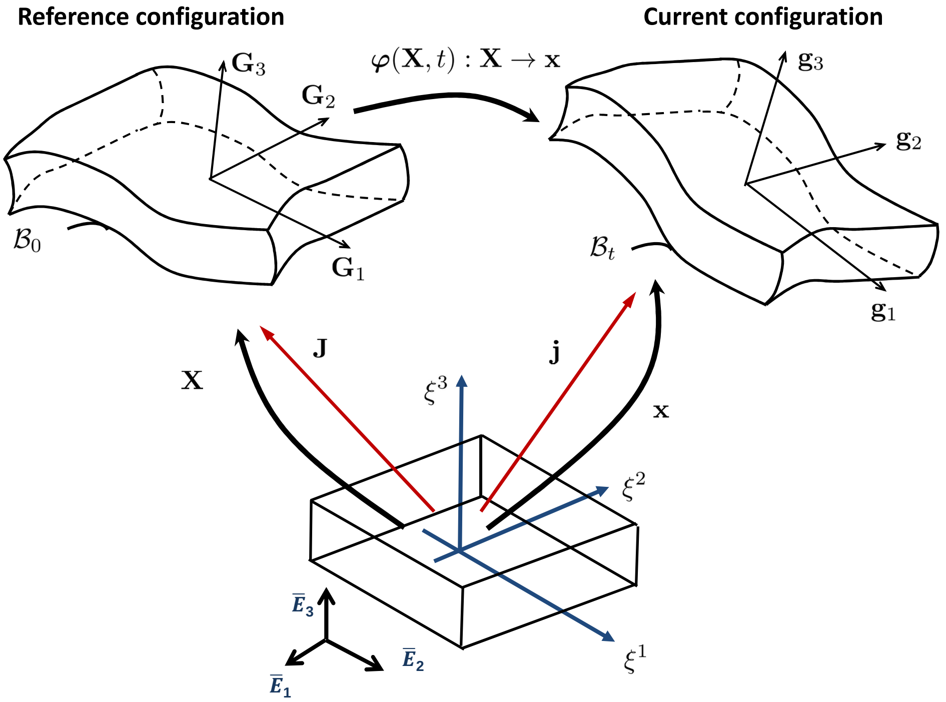

Figure 1: Shell body in the curvilinear setting. Reference $\mathcal{B}_0$ and current $\mathcal{B}_t$ configurations, whose position vectors for a material point are denoted by $\mathbf{X}$ and $\mathbf{x}$ respectively, whereas the corresponding Jacobi matrices are given by $\mathbf{J}$ and $\mathbf{j}$.

The covariant basis vectors $\mathbf{G}_i$ and $\mathbf{g}_i$ in the reference and current configurations, which represent tangents to the coordinate lines ξ^i, render

$$\mathbf{G}_i = \frac{\partial \mathbf{X}(\boldsymbol{\xi})}{\partial \xi^i}; \;\; \mathbf{g}_i = \frac{\partial \mathbf{x}(\boldsymbol{\xi})}{\partial \xi^i} = \mathbf{G}_i + \frac{\partial \mathbf{u}(\boldsymbol{\xi})}{\partial \xi^i}; \;\; i = 1,2,3; \tag{1}$$

satisfying $\mathbf{G}_i \cdot \mathbf{G}^j = \delta_i^j$ and $\mathbf{g}_i \cdot \mathbf{g}^j = \delta_i^j$, where δ_i^j is the Kronecker delta. The metric coefficients are given by: $g_{ij} = \mathbf{g}_i \cdot \mathbf{g}_j$ and $G_{ij} = \mathbf{G}_i \cdot \mathbf{G}_j$. The Jacobi matrices referred to the transformations between the parametric space in the reference, $\mathbf{J}(\boldsymbol{\xi})$, and in the current, $\mathbf{j}(\boldsymbol{\xi})$, configurations read:

$$\mathbf{J}(\boldsymbol{\xi}) = [\mathbf{G}_1, \mathbf{G}_2, \mathbf{G}_3]^{\mathrm{T}}, \quad \mathbf{j}(\boldsymbol{\xi}) = [\mathbf{g}_1, \mathbf{g}_2, \mathbf{g}_3]^{\mathrm{T}} \tag{2}$$

The respective covariant basis vectors referred to the shell midsurface ($\xi^3 = 0$) are given by

$$\mathbf{A}_\alpha = \frac{\partial \mathbf{R}(\xi^1, \xi^2)}{\partial \xi^\alpha} = \mathbf{R}_{,\alpha}\,; \;\; \mathbf{a}_\alpha = \frac{\partial \mathbf{r}(\xi^1, \xi^2)}{\partial \xi^\alpha} = \mathbf{r}_{,\alpha}\,; \;\; \alpha = 1,2, \tag{3}$$

where $\mathbf{R}(\xi^1, \xi^2)$ and $\mathbf{r}(\xi^1, \xi^2)$ denote the mid-surface shell position vectors in the reference and in the current configurations, respectively. The shell director vector in the reference configuration $\mathbf{A}_3$ is defined perpendicular to the covariant in-plane vectors $\mathbf{A}_1$ and $\mathbf{A}_2$ in the form:

$$\mathbf{A}_3(\xi^1, \xi^2) = \frac{H}{2} \frac{\mathbf{A}_1 \times \mathbf{A}_2}{|\mathbf{A}_1 \times \mathbf{A}_2|}, \tag{4}$$

where H is the initial shell thickness that is used for normalizing the out-of-plane director vector in the reference configuration.

The displacement-derived deformation gradient is defined as: $\mathbf{F}^u := \partial_{\mathbf{X}} \boldsymbol{\varphi}(\mathbf{X}, t)$, where $J = \det[\mathbf{F}^u]$ is the Jacobian of the transformation, and $\partial_{\mathbf{X}}$ identifies the partial derivative with respect to the Lagrangian frame.

We also define the displacement-derived right Cauchy-Green strain tensor, $\mathbf{C}^u$, and the Green-Lagrange strain tensor, $\mathbf{E}^u$, as

$$\mathbf{C}^u := [\mathbf{F}^u]^{\mathrm{T}} \mathbf{F}^u; \quad \mathbf{E}^u := \frac{1}{2} [\mathbf{C}^u - \mathbb{I}_2], \tag{5}$$

where $\mathbb{I}_2$ is the material covariant metric.

The compatible Green-Lagrange strain tensor can be expressed according to the following decomposition [15]:

$$E^u_{ij} = p_{ij} + \frac{H}{2} \xi^3 q_{ij} + \frac{H^2}{4} (\xi^3)^2 s_{ij}, \quad \text{with} \quad i, j = 1, 2, 3; \tag{6}$$

where p_{ij}, q_{ij} and s_{ij} denote the constant, linear and quadratic strain components in terms of the thickness coordinate ξ^3. As discussed in [15], the components s_{ij} are omitted in the sequel due to their minor contribution, especially in thin-walled applications complying with small strain conditions. Therefore, we restrict our analysis to the following form of the compatible Green-Lagrange strain tensor: $E^u_{ij} \approx p_{ij} + \frac{H}{2} \xi^3 q_{ij}$.

The definition of the constant strain components in Eq.(6) are given by

$$p_{\alpha\beta} := \frac{1}{2} [\mathbf{a}_\alpha \cdot \mathbf{a}_\beta - \mathbf{A}_\alpha \cdot \mathbf{A}_\beta], \tag{7}$$

$$p_{\alpha 3} := \frac{1}{2} [\mathbf{a}_\alpha \cdot \mathbf{A}_3 - \mathbf{A}_\alpha \cdot \mathbf{A}_3], \tag{8}$$

$$p_{33} := \frac{1}{2} [\mathbf{a}_3 \cdot \mathbf{a}_3 - \mathbf{A}_3 \cdot \mathbf{A}_3], \tag{9}$$

where $p_{\alpha\beta}$ are the membrane terms of the Kirchhoff-Love model, $p_{\alpha 3}$ identify the Reissner-Mindlin shear forces, and p_{33} is the normal strain component along the thickness direction.

Similarly, the definition of the linear strain components render

$$q_{\alpha\beta} := \frac{1}{H} [\mathbf{a}_\alpha \cdot \mathbf{a}_{3,\beta} + \mathbf{a}_\beta \cdot \mathbf{a}_{3,\alpha} - \mathbf{A}_\alpha \cdot \mathbf{A}_{3,\beta} - \mathbf{A}_\beta \cdot \mathbf{A}_{3,\alpha}], \tag{10}$$

$$q_{\alpha 3} := \frac{1}{H} [\mathbf{a}_{3,\alpha} \cdot \mathbf{a}_3 - \mathbf{A}_{3,\alpha} \cdot \mathbf{A}_3], \tag{11}$$

$$q_{33} := 0 \tag{12}$$

where $q_{\alpha\beta}$ are the curvature changes (q_{11} and q_{22}) associated with the Kirchhoff-Love model, q_{12} denotes the twisting strain component of Kirchhoff-Love formulation and $q_{\alpha 3}$ stand for the transverse shear curvatures.

The previous parametrization recalls the so-called 6-p model. This formulation yields to constant transverse normal strain components for pure bending applications since, $p_{33} \neq 0$ and $q_{33} = 0$, suffering from the well-known Poisson thickness locking when the Poisson ratio is different from zero ($\nu \neq 0$). In this work, this pathology is remedied through the use of the EAS method [15, 35, 37, 47], affecting specifically the linear transverse normal strain component q_{33} as follows:

$$E_{33} = E^u_{33} + \xi^3 \tilde{q}_{33}(\xi^1, \xi^2) = p_{33} + \xi^3 \tilde{q}_{33}(\xi^1, \xi^2). \tag{13}$$

where $\tilde{q}_{33}(\xi^1, \xi^2)$ is an incompatible linear strain term along the thickness direction, which leads to the identification of the 7-p model.

The corresponding second Piola-Kirchhoff static quantities n^{ij} and m^{ij} energetically conjugated to p_{ij} and q_{ij}, respectively, are defined as

$$n^{ij} := \int_{-1}^{+1} S^{ij} \hat{\mu} \, \mathrm{d}\xi^3; \;\; m^{ij} := \int_{-1}^{+1} S^{ij} \xi^3 \hat{\mu} \, \mathrm{d}\xi^3, \tag{14}$$

where n^{ij} and m^{ij} identify the constant (forces) and linear (moments) stress resultants per unit length, respectively, see [15, 19] for more details, and $\hat{\mu}$ stands for the transformation of the volume integrals into an integration over the shell mid-surface via the shifter tensor $\mathbf{Z} := \mathbf{G}_i \otimes \mathbf{A}^i$.

The constitutive tensor of the shell, $\mathbb{C}$, with reference to the shell mid-surface is derived through the use of the numerical integration across the thickness:

$$D_k^{ijkl} = \int_{-1}^{+1} (\xi^3)^k \mathbb{C}^{ijkl} \left(\frac{H}{2}\right)^{k+1} \hat{\mu} \, \mathrm{d}\xi^3, \;\; k = 0, 1, 2. \tag{15}$$

The constitutive operator can be expressed as a function of the thickness coordinate ξ^3 as follows:

$$\begin{bmatrix} n^{ij} \\ m^{ij} \end{bmatrix} = \begin{bmatrix} D_0^{ijkl} & D_0^{ijkl} \\ D_1^{ijkl} & D_2^{ijkl} \end{bmatrix} \begin{bmatrix} p_{ij} \\ q_{ij} \end{bmatrix}, \tag{16}$$

with

$$D_k^{ijkl} = \int_{-1}^{+1} (\xi^3)^k \mathbb{C}^{ijkl} \left(\frac{H}{2}\right)^{k+1} \hat{\mu} \, \mathrm{d}\xi^3, \;\; k = 0, 1, 2; \tag{17}$$

The stress and strain components of the model are arranged according to the following order:

$$\left[n^{ij}, m^{ij}\right] = \left[n^{11}, n^{12}, n^{13}, n^{22}, n^{23}, n^{33}, m^{11}, m^{12}, m^{13}, m^{22}, m^{23}, m^{33}\right]^{\mathrm{T}} \tag{18a}$$

$$[p_{ij}, q_{ij}] = [p_{11}, \; p_{12}, \; p_{13}, \; p_{22}, \; p_{23}, \; p_{33}, \; q_{11}, \; q_{12}, \; q_{13}, \; q_{22}, \; q_{23}, \; q_{33}]^{\mathrm{T}} \tag{18b}$$

It is worth noting that the current shell model embodies a complete description of the Green-Lagrange strain tensor, $\mathbf{E}^u$, and it is energetically conjugated second Piola-Kirchhoff stress tensor $\mathbf{S}$. This aspect allows the use of three-dimensional material laws, precluding the adoption of plane-stress assumptions as is the case in 3-p and 5-p shell models.

2.2 Three-dimensional shell parametrization

The parametrization of the shell model presented in this section is denominated as *three-dimensional shell parametrization*, which envisages a surface-oriented formulation. Fig. 2.a depicts the main attributes with regard to the kinematic arguments of the current shell model. In particular, the deformation of the reference shell surface is encompassed through the definition of six local degrees of freedom. These kinematic parameters are arranged as: (i) a vector containing the displacement of the shell surface $\mathbf{v}(\xi^1, \xi^2)$, and (ii) a difference vector $\mathbf{w}(\xi^1, \xi^2)$ which triggers the mapping of the shell director vector along the deformation process. Adopting such parametrization, the following relationships are defined:

$$\mathbf{r}(\xi^1, \xi^2) = \mathbf{R}(\xi^1, \xi^2) + \mathbf{v}(\xi^1, \xi^2); \quad \mathbf{a}_3(\xi^1, \xi^2) = \mathbf{A}_3(\xi^1, \xi^2) + \mathbf{w}(\xi^1, \xi^2). \tag{19}$$

This parametrization endows: (i) a simple linear structure with regard to the kinematic field, Eq.(19), (ii) the avoidance of rotational degrees of freedom to characterize the update of

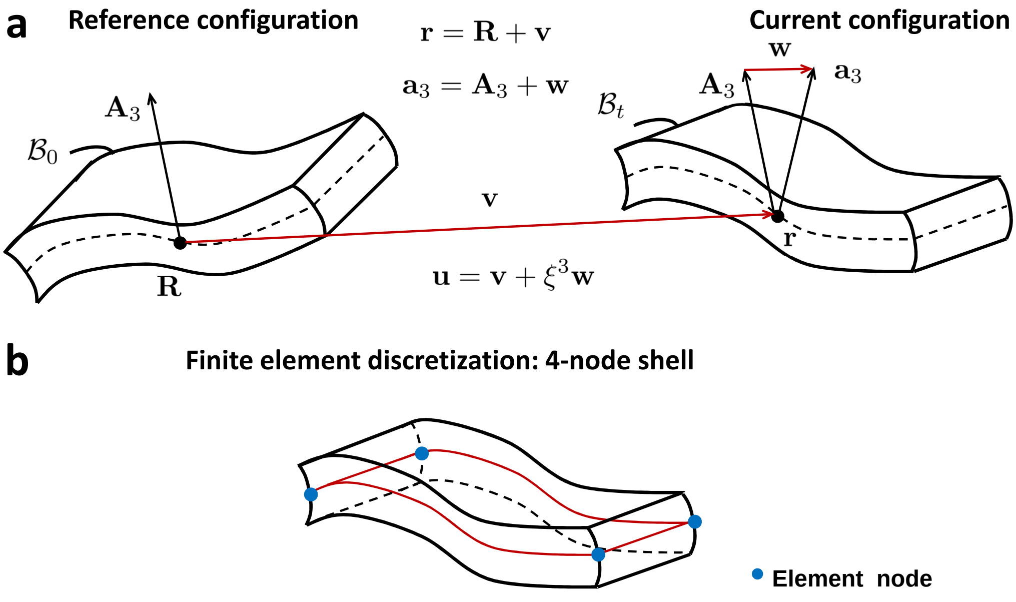

Figure 2: Three-dimensional shell parametrization. (a) Linear parametrization of the shell midsurface and the director vector. (b) Finite element discretization.

the shell director vector [16], and (*iii*) the stretching of the shell director vector in a consistent manner.

Note also that, due to the fact that in the current shell formulation the seventh degree of freedom is activated via the EAS method, the kinematic boundary conditions can be only prescribed for the six displacement components, i.e. the three components of the vectors $\mathbf{v}$ and $\mathbf{w}$ which should be defined in a consistent manner. In this sense, the boundary conditions associated with the displacement degrees of freedom of the shell midsurface $\mathbf{v} = [v_1, v_2, v_3]$ have the same physical meaning as in Classical Shell Theories (3-p and 5-p models). Conversely, the prescription of the components of the difference vector $\mathbf{w} = [w_1, w_2, w_3]$ encounters slight differences in comparison to the clamped conditions that rotational degrees of freedom introduce. In particular, the restriction of the rotation around 1-axis or 2-axis can be carried out by constraining $w_2 = 0$ and $w_1 = 0$, respectively. This can be appreciated in Fig. 3.a for the kinematic condition $\Lambda_1 = 0$ (rotation around 1-axis), for the 5–p shell model, whereas in the case of the flat plate (for simplicity) this corresponds to $w_2 = 0$ in the present 7–p shell formulation.

Furthermore, in order to have a correct interpretation of the significance of the degrees of freedom of the difference vector $\mathbf{w}$, it is necessary to conceive the shell structure similar to a three-dimensional body. This issue becomes especially relevant in the case of imposing symmetry boundary conditions, which require more careful considerations. Thus, in Fig. 3.b, the graph on the left side is related to a kinematic field including three displacements and two rotations (5–p shell model), whereas the plot on the right side corresponds to the present 7–p shell model, making use of the difference vector for this issue. Thus, the difference with regard to the restriction in the kinematic field of the same symmetry condition ($\xi^2 = 0$ is the symmetry plane) becomes evident for alternative parametrizations to updated the shell director vector.

Finally, it is worth mentioning that the restriction of the remaining sixth kinematic degree of freedom, w_3 (Fig. 3), significantly differs from the “drilling degree of freedom” that usually appears in FE packages (which introduces an artificial stiffness). In the present formulation, the local degree of freedom w_3 represents the thickness variation of the shell and should be defined in order to ensure “a proper representation of the actual physical situation”, see [19].

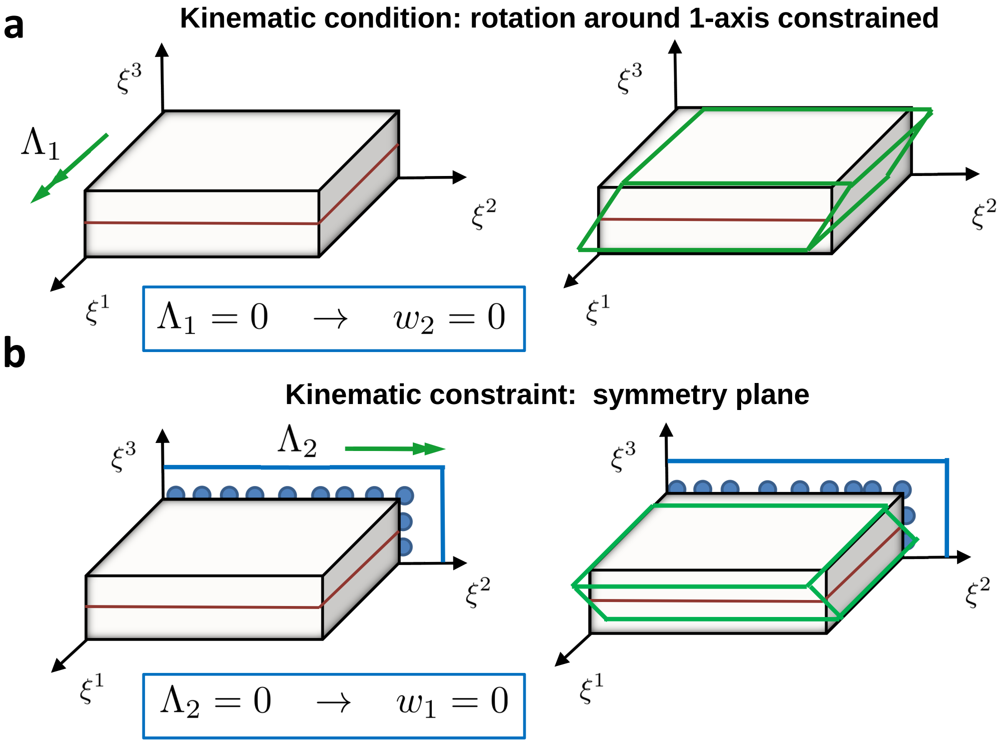

Figure 3: Characterization of the boundary conditions associated with the difference vector $\mathbf{w}$ for the three dimensional shell parametrization. (a) Kinematic condition: rotation around 1-axis is restrained. (b) Kinematic constraint: $\xi^2 = 0$ identifies a symmetry plane.

2.3 Solid shell parametrization

The second parametrization complies with the so-called solid shell concept [46]. This approach considers two displacements fields $\mathbf{v}(\xi^1, \xi^2)$ and $\mathbf{w}(\xi^1, \xi^2)$ for the description shell kinematics, relating a pair of material points on the top and bottom surfaces of the shell, see Fig. 4.a. From a mechanical perspective, the current shell parametrization contains the same geometric and kinematic configurations (only translational degrees of freedom are defined for each node in the subsequent FE formulation) of standard brick elements, but different in-plane and out-of-plane structural responses are displayed.

Accordingly, the position vector of any reference material point is given by

$$\mathbf{X}(\boldsymbol{\xi}) = \frac{1}{2}\left[1 + \xi^3\right] \mathbf{X}_t(\xi^1, \xi^2) + \frac{1}{2}\left[1 - \xi^3\right] \mathbf{X}_b(\xi^1, \xi^2), \tag{20}$$

where the position vectors $\mathbf{X}_t$ and $\mathbf{X}_b$ denote the top and bottom surfaces of the shell in the reference configuration, respectively. Eq.(20) can be rearranged as follows

$$\mathbf{X}(\boldsymbol{\xi}) = \frac{1}{2}\left[\mathbf{X}_t(\xi^1, \xi^2) + \mathbf{X}_b(\xi^1, \xi^2)\right] + \frac{1}{2}\xi^3 \left[\mathbf{X}_t(\xi^1, \xi^2) - \mathbf{X}_b(\xi^1, \xi^2)\right], , \tag{21}$$

with

$$\mathbf{R}(\xi^1, \xi^2) = \frac{1}{2}\left[\mathbf{X}_t(\xi^1, \xi^2) + \mathbf{X}_b(\xi^1, \xi^2)\right], \tag{22}$$

$$\mathbf{A}_3(\xi^1, \xi^2) = \frac{1}{2}\xi^3 \left[\mathbf{X}_t(\xi^1, \xi^2) - \mathbf{X}_b(\xi^1, \xi^2)\right]. \tag{23}$$

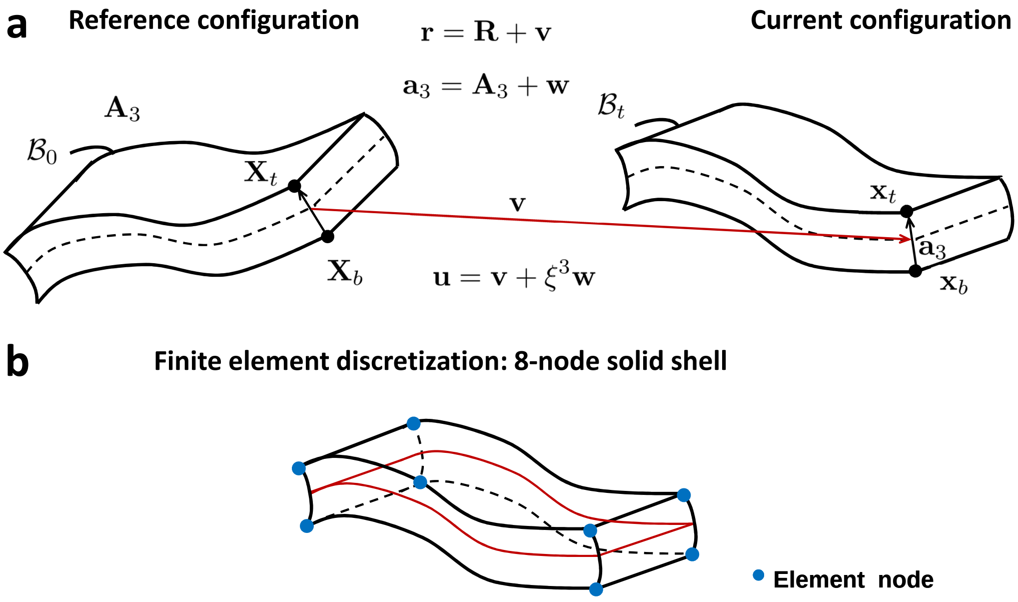

Figure 4: Solid shell parametrization. (a) Linear parametrization based on the displacements corresponding to two points located on the top and bottom surfaces of the shell. (b) Finite element discretization.

In a similar manner, the position vector in the current configuration adopts the following representation:

$$\mathbf{x}(\boldsymbol{\xi}) = \mathbf{r}(\xi^1, \xi^2) + \xi^3 \mathbf{a}_3(\xi^1, \xi^2). \tag{24}$$

Therefore, the kinematic field renders

$$\mathbf{u}(\boldsymbol{\xi}) = \mathbf{x}(\boldsymbol{\xi}) - \mathbf{X}(\boldsymbol{\xi}) = \mathbf{v}(\xi^1, \xi^2) + \xi^3 \mathbf{w}(\xi^1, \xi^2), \tag{25}$$

where $\mathbf{v}$ and $\mathbf{w}$ denote the displacement vectors of the shell midsurface and the director vector, respectively. In comparison with the alternative shell parametrization discussed in Sect.2.2, the vectors $\mathbf{v}$ and $\mathbf{w}$ for the solid shell formulation are given by

$$\mathbf{v}(\xi^1, \xi^2) = \frac{1}{2}\left[\mathbf{u}_t(\xi^1, \xi^2) + \mathbf{u}_b(\xi^1, \xi^2)\right], \tag{26}$$

$$\mathbf{w}(\xi^1, \xi^2) = \frac{1}{2}\left[\mathbf{u}_t(\xi^1, \xi^2) - \mathbf{u}_b(\xi^1, \xi^2)\right], \tag{27}$$

where $\mathbf{u}_t$ and $\mathbf{u}_b$ are the displacement vectors of the top and bottom surfaces of the shell, respectively.

The current solid shell model offers some advantages with respect to surface-based shell elements [34, 48, 47, 49]. In particular, the most appealing aspects are: (*i*) the prevention of material overlapping in highly complex structures, especially in kinks and intersections; (*ii*) the simpler adaption of FE models from geometrical data using CAD packages; (*iii*) the direct use in applications concerning double-sided contact, among many others.

It is also worth mentioning that in contrast to alternative solid shell elements, the present parametrization makes use of the so-called Dimensional Reduction Concept [38]. This is carried out through performing the numerical integration of the material law over the thickness coordinate. Therefore, this solid shell formulation is established in terms of the stress and strain resultants as described in Sect.2.1.

2.4 Shell finite element discretization

In this section, the FE discretization schemes corresponding to the parametrizations addressed in Sects. 2.2 and 2.3 are outlined. As customary in FE methods, the discretization is performed using n_e non-overlapping Lagrangian elements, such that $\mathcal{B}_0 \approx \bigcup_{e=1}^{n_e} \mathcal{B}_0^{(e)}$.

For linear displacement interpolation, the standard shape functions defined on the shell midsurface render

$$N^I = \frac{1}{4}\left(1+\xi_I^1\xi^1\right)\left(1+\xi_I^2\xi^2\right), \quad \text{with } \xi_I^1, \xi_I^2 = \pm 1, \quad \text{and } I = 1,2,3,4. \tag{28}$$

According to the isoparametric concept, both the *three-dimensional shell* and the *solid shell* parametrizations permit the interpolation of the reference and current geometry as follows:

$$\mathbf{X} = \mathbf{R} + \xi^3\mathbf{A}_3 \approx \sum_{I=1}^{4} N^I\mathbf{R}^I + \xi^3 N^I \mathbf{A}_3^I = \mathbf{N}\mathbf{R}^e + \xi^3\mathbf{N}\mathbf{A}_3^e \tag{29}$$

$$\mathbf{x} = \mathbf{r} + \xi^3\mathbf{a}_3 \approx \sum_{I=1}^{4} N^I\mathbf{r}^I + \xi^3 N^I \mathbf{a}_3^I = \mathbf{N}\mathbf{r}^e + \xi^3\mathbf{N}\mathbf{a}_3^e. \tag{30}$$

In Eqs.(29)–(30), $\mathbf{N}$ corresponds to the shape-function operator at the element level; $\mathbf{R}^I$ and $\mathbf{r}^I$ stand for the discrete midsurface position vectors in the reference and in the current configurations, respectively, whose corresponding operators at the element level are denoted by $\mathbf{R}^e$ and $\mathbf{r}^e$; $\mathbf{A}_3^I$ and $\mathbf{a}_3^I$ are the reference and current nodal director vectors, respectively, which are arranged into the operators $\mathbf{A}_3^e$ and $\mathbf{a}_3^e$ at the element level.

As discussed above, the two shell parametrizations herein considered lead to different element topologies. On the one hand, the *three-dimensional shell* formulation endows a 4-node shell element (Fig. 2.b) whereby special attention to the definition of the shell director vector should be paid [38], see A. On the other hand, the *solid shell* parametrization results in a 8-node shell element, (Fig. 4.b), leading to a direct definition of the shell director vector by exploiting the position vectors of the nodes at the top and bottom surfaces of the shell [39].

The interpolation of the displacement field $\mathbf{u}$, its variation $\delta\mathbf{u}$, and its increment $\Delta\mathbf{u}$ read:

$$\mathbf{u} \approx \tilde{\mathbf{N}}\mathbf{d}; \quad \delta\mathbf{u} \approx \tilde{\mathbf{N}}\delta\mathbf{d}; \quad \Delta\mathbf{u} \approx \tilde{\mathbf{N}}\Delta\mathbf{d}, \tag{31}$$

with

$$\tilde{\mathbf{N}}\mathbf{d} = \mathbf{N}\mathbf{v} + \xi^3\mathbf{N}\mathbf{w}, \tag{32}$$

and

$$\tilde{\mathbf{N}} = \begin{bmatrix} N^1 & 0 & 0 & \xi^3N^1 & 0 & 0 & \cdots & N^4 & 0 & 0 & \xi^3N^4 & 0 & 0 \\ 0 & N^1 & 0 & 0 & \xi^3N^1 & 0 & \cdots & 0 & N^4 & 0 & 0 & \xi^3N^4 & 0 \\ 0 & 0 & N^1 & 0 & 0 & \xi^3N^1 & \cdots & 0 & 0 & N^4 & 0 & 0 & \xi^3N^4 \end{bmatrix} \tag{33}$$

The interpolation scheme given in Eq.(32) also holds for the variation and increment of the displacement field. In the previous expressions, $\mathbf{d}$ represents the nodal displacement vector at the element level, whilst the operator $\tilde{\mathbf{N}}$ also depends upon the particular shell parametrization, see [38, 39] for further details.

The displacement derived strain field $\mathbf{E}^u$, its variation $\delta\mathbf{E}^u$ and its increment $\Delta\mathbf{E}^u$ are interpolated through a suitable *compatibility* operator $\mathbf{B}$ as follows:

$$\mathbf{E}^u \approx \mathbf{B}(\mathbf{d})\mathbf{d}, \quad \delta\mathbf{E}^u \approx \mathbf{B}(\mathbf{d})\delta\mathbf{d}, \quad \Delta\mathbf{E}^u \approx \mathbf{B}(\mathbf{d})\Delta\mathbf{d}. \tag{34}$$

The operator $\mathbf{B}$ contains the derivatives of the shape functions with respect to the global coordinate setting, whose particular forms for both shell parametrizations under analysis are detailed in B.

3 The EAS method and constitutive formulation

3.1 Variational basis of the EAS method

In this section, we discuss the variational basis for the use of the EAS method within the context of geometrically nonlinear theory. The starting point in the corresponding derivation concerns the mixed Hu-Washizu variational principle adopting a total Lagrangian formulation [25, 50].

In line with [15], the additive decomposition of the total Green-Lagrange strain tensor into a displacement-derived $\mathbf{E}^u$ and an incompatible $\tilde{\mathbf{E}}$ counterparts, $\mathbf{E} = \mathbf{E}^u + \tilde{\mathbf{E}}$, is herewith adopted. The resulting variation of the Hu-Washizu functional reads [47]:

$$\delta\Pi(\mathbf{u}, \delta\mathbf{u}, \tilde{\mathbf{E}}, \delta\tilde{\mathbf{E}}) = \int_{\mathcal{B}_0} \mathbf{S} : \delta\mathbf{E}^u \, \mathrm{d}\Omega + \int_{\mathscr{B}_0} \mathbf{S} : \delta\tilde{\mathbf{E}} \, \mathrm{d}\Omega - \delta\Pi_{\text{ext}} = \delta\Pi_{\text{int}} - \delta\Pi_{\text{ext}} = 0, \;\; \forall\delta\mathbf{u} \in \mathcal{V}, \; \delta\tilde{\mathbf{E}} \in \mathcal{V}^{\tilde{E}}, \tag{35}$$

where $\mathcal{V} = \{\delta\mathbf{u} \in [H^1(\mathcal{B}_0)] : \delta\mathbf{u} = \mathbf{0} \text{ on } \partial\mathcal{B}_{0,u}\}$ stands for any kinematic admissible virtual displacements, which satisfy the essential boundary conditions; $\mathcal{V}^{\tilde{E}} = [L_2(\mathcal{B}_0)]$ is the admissible space corresponding to the incompatible strains, whilst $\delta\Pi_{\text{int}}$ and $\delta\Pi_{\text{ext}}$ identifying the internal and external contributions, respectively. The stress field is removed from Eq.(35) by imposing the so-called orthogonality condition between the interpolation spaces associated with the stress and the enhanced strain fields [50, 25]

The consistent linearization of the nonlinear system in Eq.(35) is given by

$$\Delta\delta\Pi(\mathbf{u}, \delta\mathbf{u}, \Delta\mathbf{u}, \tilde{\mathbf{E}}, \delta\tilde{\mathbf{E}}, \Delta\tilde{\mathbf{E}}) = \int_{\mathscr{B}_0} \Delta\mathbf{S} : \delta\mathbf{E}^u \, \mathrm{d}\Omega + \int_{\mathscr{B}_0} \mathbf{S} : \Delta\delta\mathbf{E}^u \, \mathrm{d}\Omega + \int_{\mathscr{B}_0} \Delta\mathbf{S} : \delta\tilde{\mathbf{E}} \, \mathrm{d}\Omega, \tag{36}$$

where the linearized virtual Green-Lagrange adopts the form

$$\Delta\delta\mathbf{E}^u = \frac{1}{2}\left[\delta\mathbf{g}_i \cdot \Delta\mathbf{g}_j + \Delta\mathbf{g}_i \cdot \delta\mathbf{g}_j\right] \mathbf{G}^i \otimes \mathbf{G}^j, \tag{37}$$

and the corresponding linearization of the stress field renders:

$$\Delta\mathbf{S} = \frac{\partial\mathbf{S}}{\partial\mathbf{E}^u} : \Delta\mathbf{E}^u + \frac{\partial\mathbf{S}}{\partial\tilde{\mathbf{E}}} : \Delta\tilde{\mathbf{E}}. \tag{38}$$

The partial derivative of the stress tensor with respect to the strain tensor yields to the definition of the fourth-order constitutive operator $\mathbb{C} := \partial\mathbf{S}/\partial\mathbf{E} = \partial^2_{\mathbf{EE}}\Psi$, which is particularized to layered composites and FGMs in Sect.3.3.

3.2 Interpolation of the incompatible strains

The interpolation of the incompatible strain field is expressed in terms of the operator $\mathbf{M}(\boldsymbol{\xi})$ that is designed to alleviate the following locking pathologies: (*i*) membrane and in-plane shear locking, (*ii*) volumetric locking, and (*iii*) Poisson thickness locking. Transverse shear and trapezoidal locking are remedied by means of the ANS method as described in C.

The incompatible strain field $\tilde{\mathbf{E}}$, its variation $\delta\tilde{\mathbf{E}}$ and its increment $\Delta\tilde{\mathbf{E}}$ can be approximated at the element level as follows:

$$\tilde{\mathbf{E}} \approx \mathbf{M}(\boldsymbol{\xi})\boldsymbol{\varsigma}, \;\; \delta\tilde{\mathbf{E}} \approx \mathbf{M}(\boldsymbol{\xi})\delta\boldsymbol{\varsigma}, \;\; \Delta\tilde{\mathbf{E}} \approx \mathbf{M}(\boldsymbol{\xi})\Delta\boldsymbol{\varsigma}, \tag{39}$$

being $\boldsymbol{\varsigma}$ the vector of the internal strain parameters at the element level.

As discussed in [38], the incompatible strains are defined via the operator $\tilde{\mathbf{M}}$, which is constructed within the parametric space $\boldsymbol{\xi} = \{\xi^1, \xi^2, \xi^3\}$. Therefore, since that since the operator

$\mathbf{M}$ is expressed in the global setting, a suitable transformation between the operators $\tilde{\mathbf{M}}$ and $\mathbf{M}$ is required. In this concern, the enhanced part of the strain field in different basis is given by

$$\tilde{\mathbf{E}} = \tilde{E}_{ij}(\mathbf{G}^i \otimes \mathbf{G}^j) = \tilde{\epsilon}^0_{kl}(\mathbf{A}^k_0 \otimes \mathbf{A}^l_0), \tag{40}$$

where $\tilde{\epsilon}^0_{kl}$ represent these components at the element center whose internal basis are denoted as $\mathbf{A}_0$. After some manipulations [44], the enhanced strain tensor takes the form:

$$\tilde{\boldsymbol{E}} = (\mathbf{T}_0)^{-\mathrm{T}} \left[\frac{\det\mathbf{J}_0}{\det\mathbf{J}}\right] \tilde{\mathbf{M}}\boldsymbol{\varsigma} = \mathbf{M}\boldsymbol{\varsigma}, \tag{41}$$

where $\mathbf{T}_0$ stands for a transformation matrix between the basis at the element centre and the contravariant basis system at the integration points, and $\mathbf{J}$ and $\mathbf{J}_0$ identify the Jacobian and its evaluation at the element center, respectively.

With regard to the form of the operator $\tilde{\mathbf{M}}$, in the current research, a particular version considering 22 enhanced strains is chosen, see [38, 39]. According to the strain arrangement given in Eq.(18), this matrix can be expressed in the strain resultants space (p_{ij}, q_{ij}) as follows:

$$\tilde{\mathbf{M}} = \begin{bmatrix} \tilde{\mathbf{M}}_p \\ \tilde{\mathbf{M}}_q \end{bmatrix} = \begin{bmatrix} \tilde{\mathbf{M}}_7 & \mathbf{0}_7 & \mathbf{0}_4 & \mathbf{0}_4 \\ \mathbf{0}_7 & \tilde{\mathbf{M}}_7 & \tilde{\mathbf{M}}_4^{q_{33}} & \tilde{\mathbf{M}}_4 \end{bmatrix} \tag{42}$$

with

$$\tilde{\mathbf{M}}_7 = \begin{bmatrix} \xi^1 & 0 & 0 & 0 & \xi^1\xi^2 & 0 & 0 \\ 0 & 0 & \xi^1 & \xi^2 & 0 & 0 & \xi^1\xi^2 \\ 0 & 0 & 0 & 0 & 0 & 0 & 0 \\ 0 & \xi^2 & 0 & 0 & 0 & \xi^1\xi^2 & 0 \\ 0 & 0 & 0 & 0 & 0 & 0 & 0 \\ 0 & 0 & 0 & 0 & 0 & 0 & 0 \end{bmatrix} \tag{43}$$

$$\tilde{\mathbf{M}}_4 = \begin{bmatrix} 0 & 0 & 0 & 0 \\ 0 & 0 & 0 & 0 \\ \xi^1 & \xi^1\xi^2 & 0 & 0 \\ 0 & 0 & 0 & 0 \\ 0 & 0 & \xi^2 & \xi^1\xi^2 \\ 0 & 0 & 0 & 0 \end{bmatrix} \quad \tilde{\mathbf{M}}_4^{q_{33}} = \begin{bmatrix} 0 & 0 & 0 & 0 \\ 0 & 0 & 0 & 0 \\ 0 & 0 & 0 & 0 \\ 0 & 0 & 0 & 0 \\ 0 & 0 & 0 & 0 \\ 1 & \xi^1 & \xi^2 & \xi^1\xi^2 \end{bmatrix}, \tag{44}$$

being $\mathbf{0}_n$ null matrix of order $6 \times n$. Note that the matrix $\tilde{\mathbf{M}}_4^{q_{33}}$ only affects the strain component q_{33}, leading to the 7-p shell model [19].

The insertion of the interpolation schemes introduced in Eqs.(31) and (39) corresponding to the displacements and the incompatible strains, respectively, into the residual and linearized forms given in Eqs.(35)-(36) leads to a coupled nonlinear problem with two independent fields. However, the incompatible strains can be removed at element level through the exploitation of a static condensation procedure. At this point, it is important to remark that the number of EAS parameters under consideration has a notable role with regard to the numerical efficiency of the formulation, see [38, 39] for further details. Therefore, it is interesting to optimize the number of EAS parameters depending on the application under analysis and the FE mesh.

3.3 Constitutive formulation

Two basic constitutive models for composite materials complying with the Kirchhoff-Saint-Venant formulation (with a linear relationship $\mathbf{S} = \mathbb{C} : \mathbf{E}$) are considered for both parametrizations introduced above. The first material type is used to model layered composite shells (Sect. 3.3.1) through the adoption of the ESL approach, whereas the second constitutive model refers to power-based functionally graded materials (Sect. 3.3.2).

3.3.1 Layered composite shells

From a mechanical point of view, laminated CFRP (Carbon Fiber Reinforced Polymer) composites are modeled in this study through the advocation of the ESL approach, which is especially suitable for laminates with similar stiffness values between the composing layers. Henceforth, two basic modeling assumptions are considered: (*i*) orthotropic material law for each lamina, and (*ii*) perfectly bonded interlaminar behavior. Therefore, the constitutive tensor can be computed by accounting for the dependence of the stacking sequence of the laminate over the shell thickness coordinate ξ^3 (Fig. 5.a):

$$\mathbb{C}(\xi^3) = \begin{cases} \mathbb{C}_{N_L} & \bar{\xi}^3_{N_L} \leq \xi^3 \leq \bar{\xi}^3_{N_L+1} = +1 \\ \mathbb{C}_{N_L-1} & \bar{\xi}^3_{N_L-1} \leq \xi^3 \leq \bar{\xi}^3_{N_L} \\ .... & ..... \\ \mathbb{C}_2 & \bar{\xi}^3_2 \leq \xi^3 \leq \bar{\xi}^3_3 \\ \mathbb{C}_1 & -1 = \bar{\xi}^3_1 \leq \xi^3 \leq \bar{\xi}^3_2 \end{cases} . \tag{45}$$

The thickness coordinate in Eq.(45) varies in the range $\xi^3 \in [-1, +1]$ after its normalization by the total laminate thickness H, whereby $H = \sum_{i=1}^{N_L} H_i$, being N_L the total number of laminae and H_i the individual ply thickness.

The shell coordinate midsurface of each layer is denoted as ξ^3_i and is given by

$$\xi^3_i = -1 + \frac{H_i}{H} + \frac{2}{H} \sum_{j=1}^{i-1} H_j \quad i{=}1{,}...{,}N_L \tag{46}$$

In order obtained the resulting weighted averaged material properties of the complete laminate, the constitutive temrs introduced in Eq.(15) take the form:

$$D_k^{mnop} = \sum_{i=1}^{N_L} \frac{H_i}{H^{k+1}} \int_{-1}^{1} \hat{\mu}_{\zeta_i} \left[-H - H_i(1-\zeta_i) + 2\sum_{j=1}^{i} H_j \right] \mathbb{C}_i^{mnop} \, \mathrm{d}\zeta_L, \;\; k = 0, 1, 2; \tag{47}$$

where i identifies the current lamina, and ξ^3 is defined as:

$$\xi^3 = -1 + \frac{1}{H} \left[-H_L(1-\zeta_L) + 2\sum_{i=1}^{L} H_i \right] \tag{48}$$

3.3.2 Functionally graded isotropic shells

The second constitutive model herewith considered regards power-based functionally graded materials (FGMs). These materials are characterized by the smooth variation of the the volume fractions of two or more constituents, usually along the thickness direction [39, 51, 52]. In a general sense, the variation of the material properties over the shell thickness is governed by the following classical mixture rule:

$$\iota(\xi^3) = \iota_m f_m + \iota_c f_c \tag{49}$$

where the subscripts m and c denote the metallic and the ceramic components respectively, f is the volume fraction of the corresponding phase, and ι is a generic material property. Adopting a power law form, the corresponding volume fractions of both constituents are given by

$$f_c = \left[\frac{\xi^3}{H} + \frac{1}{2} \right]^n \tag{50}$$

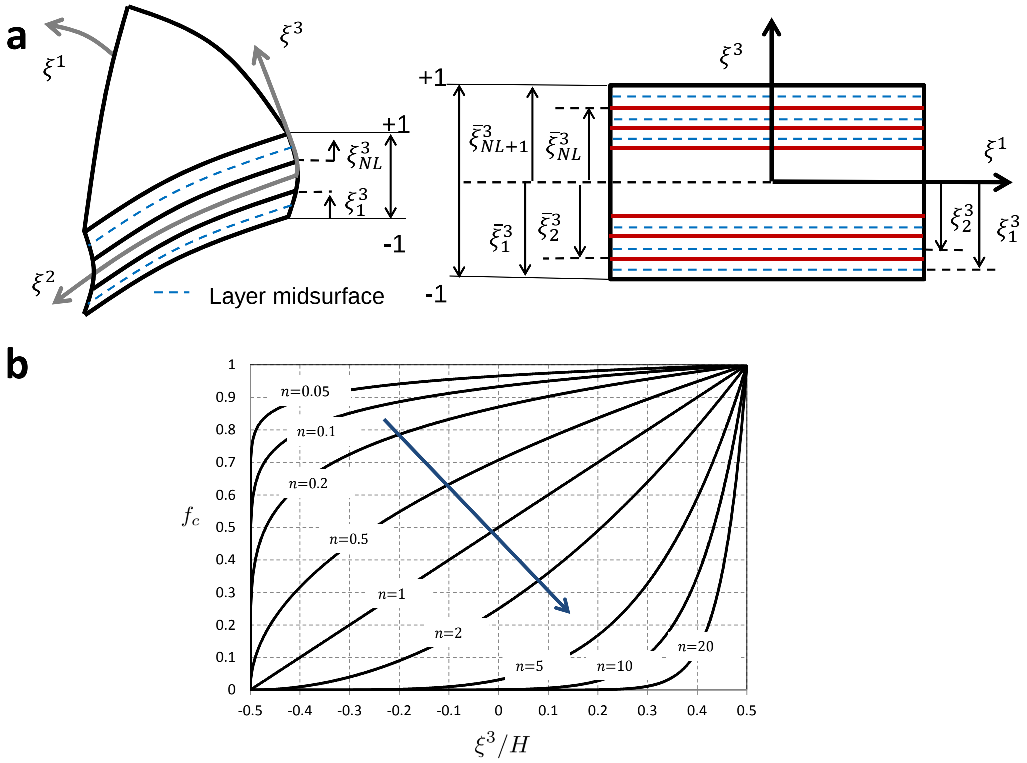

Figure 5: Constitutive models. (a) Laminated shell structure: local layer setting and definition of auxiliary natural coordinates over the shell thickness $\bar{\xi}^3_i$. (b) Power-based functionally graded composites: variation of the volume fraction of ceramic material f_c through the thickness coordinate ξ^3.

$$f_m = 1 - f_c, \tag{51}$$

where n represents a volume fraction exponent.

Recalling standard arguments [53], the second Piola-Kirchhoff stress tensor, $\mathbf{S}(\xi^3)$, and the constitutive tensor, $\mathbb{C}(\xi^3)$, as a function of ξ^3 read

$$\mathbf{S}(\xi^3) = \partial_{\mathbf{E}}\Psi(\xi^3) = S^{ij}(\xi^3)\mathbf{G}_i \otimes \mathbf{G}_j, \tag{52}$$

$$\mathbb{C}(\xi^3) = \partial^2_{\mathbf{EE}}\Psi(\xi^3) = \mathbb{C}^{ijkl}(\xi^3)\mathbf{G}_i \otimes \mathbf{G}_j \otimes \mathbf{G}_k \otimes \mathbf{G}_l. \tag{53}$$

In this regard, the value of the exponent n rules the composition of the constitutive model, see the evolution of the ceramic constituent volume fraction within the shell body for different values of n in Fig. 5.b. Thus, the case $n = 0$ identifies a fully ceramic structure, whereas when n tends to infinity a fully metallic body is obtained.

4 Numerical examples

In this section, several geometrically linear and nonlinear examples are presented in order to assess the performance of the surface-based (three dimensional shell) and the solid shell formulations of the 7-parameter shell model for their application to layered CFRP and functionally graded power-based composite structures. In the sequel, the three dimensional shell and the solid shell parametrizations are labeled as TShell7p and SShell7p, respectively. All the computations are performed using the commercial FE package ABAQUS. Both element formulations are implemented in such code using the user-defined capability `UEL` according to the algorithmic treatment described in [38]. For comparison purposes for isotropic examples, numerical solutions obtained from the computations are compared with the ABAQUS shell elements S4R and S4 for the three dimensional shell models, whereas the ABAQUS continuum shell SC8R is employed to evaluate the performance of the present solid shell formulation.

4.1 Scordelis–Lo roof under volume force

The first linear benchmark problem is known as the Scordelis–Lo roof test, which was conceived for testing the membrane and bending performance of the elements [56]. A semi–cylindrical shell mounted over two end diaphragms at the curved edges is subjected to self-weight loading conditions, with a density value of $\rho = 360$ N/mm^3, see Fig. 6.a. The geometric data for the problem are: roof length $L = 50$ mm, radius $R = 25$ mm and thickness $t = 0.25$ mm. The material parameters correspond to isotropic mechanical behavior with a Young's modulus $E = 4.32 \times 10^8$ N/mm^2 and Poisson ratio $\nu = 0$.

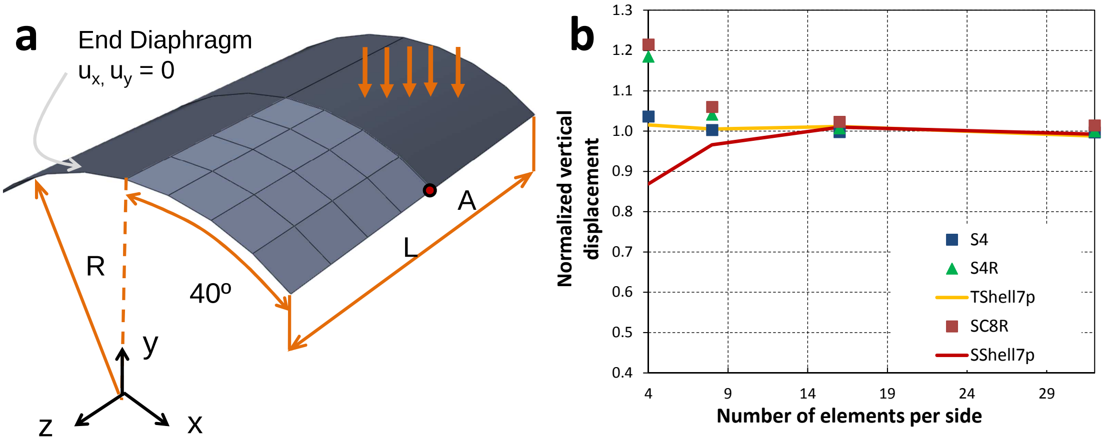

Figure 6: Scordelis–Lo roof under volume force. (a) Geometry and load conditions. (b) Linear analysis: comparison between ABAQUS S4, S4R and SC8R elements and TShell7p and SShell7p elements.

One quarter of the roof is modeled due to symmetric conditions, the structure being discretized using 4, 8, 12 and 16 elements per side. The boundary conditions at the end diaphragms are given by u_x, $u_y = 0$, accordingly to the frame represented in Fig. 6.a. The reference solution adopted for the vertical displacement of the point located at the center of the free edge (A) is: $u_y(A) = -0.3024$ mm [61]. In Fig. 6.b, the normalized vertical displacements at the point A for the current three-dimensional and the solid shell elements and for the ABAQUS elements S4, S4R and SC8R are represented. Observing this plot, it is clearly evident the very good agreement achieved between both 7–parameter shell elements and the ABAQUS elements, and also in comparison with the reference solution under consideration.

4.2 Pinched hemispherical shell with 18° hole

This example illustrates a classical double-curved shell problem. It serves to test the ability of FE shell formulations to reproduce membrane and bending states correctly. This benchmark application has been employed for validation purposes by different authors, see [16, 36, 23, 15, 57], just to name a few of them. The results can be found tabulated in Sze et al. [58] for ABAQUS elements.

The example considers an isotropic hemispherical shell with an 18° hole on the top, which is subjected to two inward and two outward forces perpendicular to each other, see Fig. 7.a. The geometric data are: radius $R = 10$ m and thickness $t = 0.04$ m. The material parameters are: Young's modulus $E = 68.25 \times 10^6$ Pa and Poisson ratio $\nu = 0.3$. Due to the symmetry of the problem, only one quarter of the structure is modeled. In the case of the geometrically linear applications, different meshes were considered, in particular 4, 8, 16 and 32 elements per side.

A schematic representation of one of the boundary conditions applied to the model is shown in Figs. 7.b and 7.c for the TShell7p and SShell7p parametrizations, respectively. In this concern, note that, on the one hand, the TShell7p and S4 and S4R elements define one node on the shell midsurface, making it possible to assign the load to this node. On the other hand, the SShell7p elements provide a couple of nodes placed on the top and bottom surfaces of the element, therefore the external pinching forces are distributed among these nodes and the related displacements are averaged during the postprocessing stage.

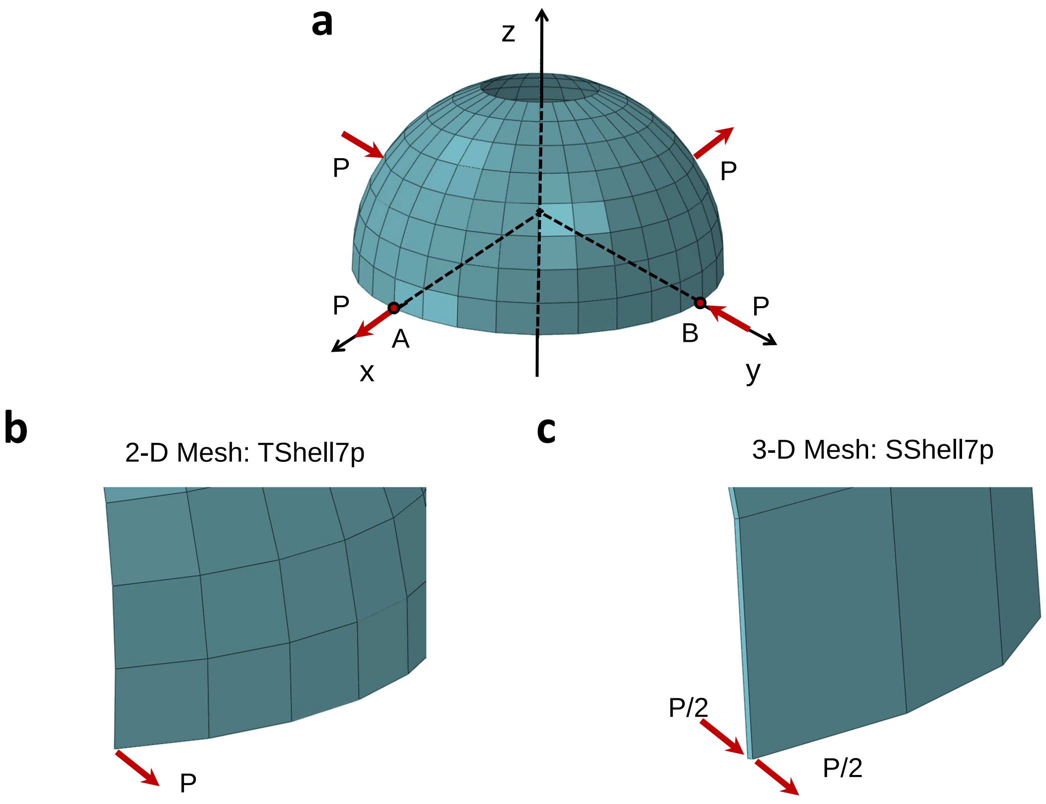

Figure 7: Pinched hemispherical shell with 18° hole. (a) Geometry and material data. (b) Detail of applied load for the TShell7p parametrization. (c) Detail of applied load for the SShell7p parametrization.

4.2.1 Linear analysis

Through the application of a concentrated force $P_{max} = 1$ N, a study of the convergence of the solution with respect to the reference value $u_y^{(A)} = 0.094$ mm provided by Simo et al. [60] is presented in Fig. 8.a and is compared with the standard ABAQUS elements. In these graphs, the normalized displacement with respect to the reference solution of the point A is plotted versus the number of elements per side, whereby a very good agreement between the results reported and the reference solutions can be appreciated.

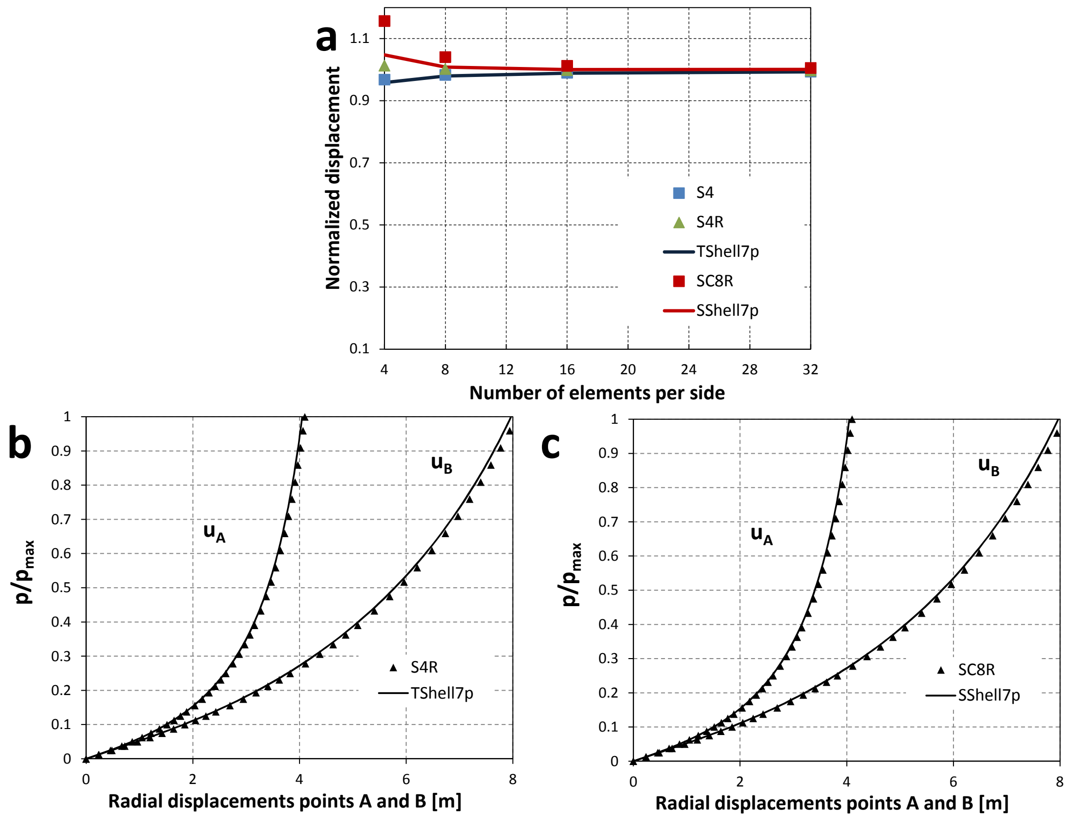

Figure 8: Pinched hemispherical shell with 18° hole. Comparison between ABAQUS S4, S4R elements and TShell7p and SShell7p elements. (a) Linear analysis. (b) Comparison between ABAQUS S4R element and TShell7p element: geometrically Nonlinear application. (c) (b) Comparison between ABAQUS SC8R element and SShell7p element: geometrically Nonlinear application.

Additionally, the results here obtained are reported in Table 1 and are correlated with those corresponding to other element formulations due to Kasper and Taylor [29] (mixed enhanced strain element) and Schwarze and Reese [61] (reduced integration, EAS and ANS element). The current results exhibit a closer agreement with respect to the reference solutions for all the meshes densities in comparison to the alternative shell formulations cited above.

N_e	TShell7p	SShell7p	Kasper and Taylor [29]	Schwarze and Reese [61]
4	0.959	1.047	0.039	1.043
8	0.979	1.008	0.732	1.002
16	0.988	1.003	0.989	0.993
32	0.993	1.0001	0.998	0.994

Table 1: Pinched hemispherical shell with 18° hole: normalized displacements. N_e denotes the number of elements per side. The results were obtained using the following procedures to avoid locking: 22 parameters by means of the EAS Method and the ANS Method for transverse shear and curvature thickness locking.

4.2.2 Geometrically nonlinear analysis

In the case of the geometrically nonlinear application, each of the applied loads reach a value of $P_{max} = 400$ N [16]. Figs. 8.b and 8.c depict the numerical correlation obtained using a mesh density of 16×16 elements in comparison with the ABAQUS elements S4R and SC8R for the TShell7p and SShell7p parametrizations, respectively. In these plots, an excellent accuracy with respect to the reference solutions can be observed.

From the resolution process standpoint, due to the different physical meaning of the nodal degrees of freedom 4, 5 and 6 for the TShell7p approach (corresponding to the difference vector $\mathbf{w}$) in comparison to the standard ABAQUS elements, severe convergence problems are found in achieving equilibrium solutions. To overcome such difficulties, the arc-length Riks Method implemented in ABAQUS Standard is employed, for which 458 time steps are required in order to achieve the final load. In contrast to this, the SShell7p formulation allows a load control time step to be employed without finding severe convergence difficulties in achieving equilibrium solutions. Therein, an initial and a maximum increment load size of 5% of the final load is selected, requiring 92 steps to achieve the final load with a minimum load increment equal to 0.7031%.

4.3 Pinched cylinder with end diaphragms

Another well-known isotropic benchmark problem for cylindrical shells is the pinched cylinder with end diaphragms. Due to symmetry of the structure, only one one-eighth of the cylinder is modeled. The geometrical characteristic of this example are portrayed in Fig. 9.a, with radius $R = 300$ mm, length $L = 600$ mm, thickness $t = 3$ mm for the geometrically linear case, whereas radius $R = 100$ mm, length $L = 200$ mm, thickness $t = 1$ mm defines the geometrically nonlinear case (note that the geometrical ratios R/L and t/L are equivalent between both cases). The structure is symmetrically compressed by the action of two opposite loads on the midsurface of the cylinder ($P = 12000$ N), see Fig. 9.a. The material properties are: Young's modulus $E = 30 \times 10^3$ Pa and Poisson ratio $\nu = 0.3$.

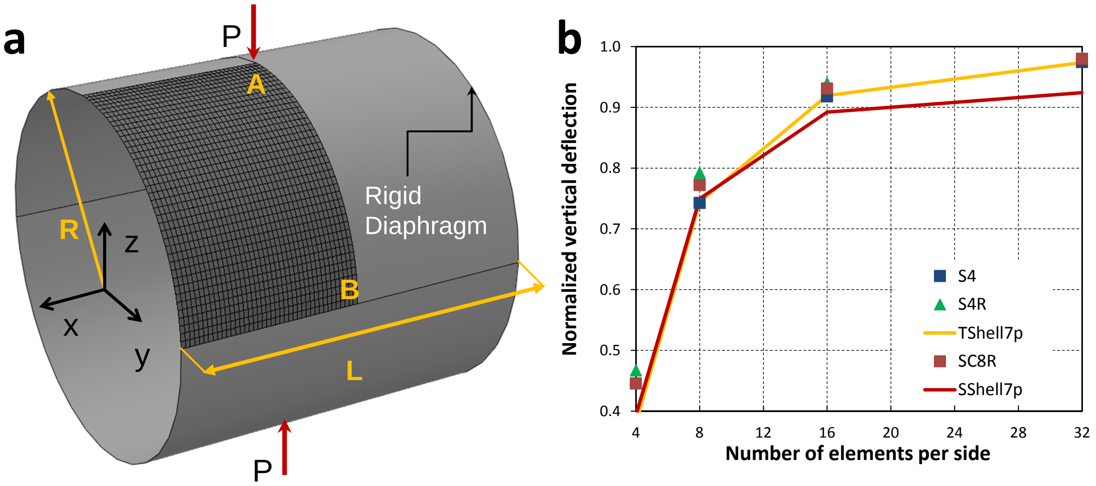

Figure 9: Pinched Cylinder with end diaphragms. Geometry and material data

The structure is dominated by an inextensional bending and complex membrane states which may cause membrane locking. Moreover, as a consequence of the highly curved and thin geometry, curvature thickness and transverse shear locking effects take place. Therefore, this example serves to test the elements performances under one of the most severe mechanical conditions [57].

4.3.1 Linear analysis

For the geometrically linear applications, four different meshes are employed: 4, 8, 16 and 32 elements per side, i.e along AB. Fig. 9.b depicts the normalized radial displacement of the point A with respect to the reference solution ($w_A = 1.8541 \times 10^{-5}$ mm, against the number of elements per side [59]). As can be seen in the graph, the ABAQUS elements S4R and SC8R and the TShell7p and SShell7p elements exhibit a poor accuracy for coarse meshes. A very satisfactory convergence for both 7p formulations is achieved once the mesh refinement is performed, especially for the TShell7p element which offers a very close performance to the elements of ABAQUS. A specific deviation of around 3% with respect to the reference solution is obtained for the SShell7p case.

4.3.2 Geometrically nonlinear analysis

In the case where geometrical nonlinearities are taken into consideration, one-eighth of the cylinder is modeled using a mesh 40×40 shell elements, being adequate for the different element typologies under study, namely, the TShell7p and SShell7p elements and the ABAQUS elements S4R and SC8R [58].

For the TShell7p element, the convergence difficulties mentioned above are again found along the loading process. Note that from the structural standpoint, this application does not exhibit significant instabilities, and therefore the convergence problems along the resolution process can be attributed to: (i) the different mechanical significance of the nodal degrees of freedom 4, 5 and 6 in comparison with those of the standard shell elements implemented in ABAQUS, see [38] for a more comprehensive discussion, and (ii) the specific numerical tolerances to evaluate the residual terms. In order to overcome such difficulties, computations are repeated using a displacement control scheme, taking the initial and the maximum load step size as 1% of the final load, and using different magnitudes of the artificial damping ABAQUS's `*stabilize` option (labeled with the suffix St). Figs. 10.a and 10.b depict the load against the radial deflection of the points A and B obtained using the TShell7p element in comparison with the numerical solution provided by the ABAQUS element S4R. In this diagram it is observed that the smaller values of the ABAQUS's `*stabilize` option are set, the closer agreement with the ABAQUS element is achieved. Thus, the discrepancies between the results from the TShell7p element with those corresponding to the reference solution are ascribed to the introduction of the artificial damping in the numerical resolution process.

Differing from the previous case, for the SShell7p element, a nonlinear procedure using a displacement control scheme, where the initial and the maximum load step size correspond to 1% of the final load, is successfully used. Figs. 10.c and 10.d depict the radial displacements of the points A and B. These results are compared with the solutions obtained with the ABAQUS element SC8R, exhibiting an excellent level of agreement.

4.4 Cantilever beam under distributed end load

4.4.1 Isotropic material law

This problem consists of a cantilever beam under distributed end forces, see Fig. 11.a (where u and w denote the tip displacements along the x and z axis, respectively). This classical application allows the out-of-plane bending performance of the elements implemented to be evaluated. The present example has been extensively employed as a popular nonlinear benchmark problem by a large number of authors, see [16, 23, 49] among many others. The results are tabulated in Sze et al. [58] for meshes 8×1 (identified by Mesh 8) and 16×1 (identified by Mesh 16), which adequate for the first-order reduced integration ABAQUS elements.

In the present analysis, the structure is discretized using 8 in-plane elements and one element over the thickness direction. The geometrical data are: length $L = 10$ m, width $b = 1$ m and thickness $t = 0.1$ m. The material properties correspond to: $E = 1.2$ MPa and $\nu = 0$.

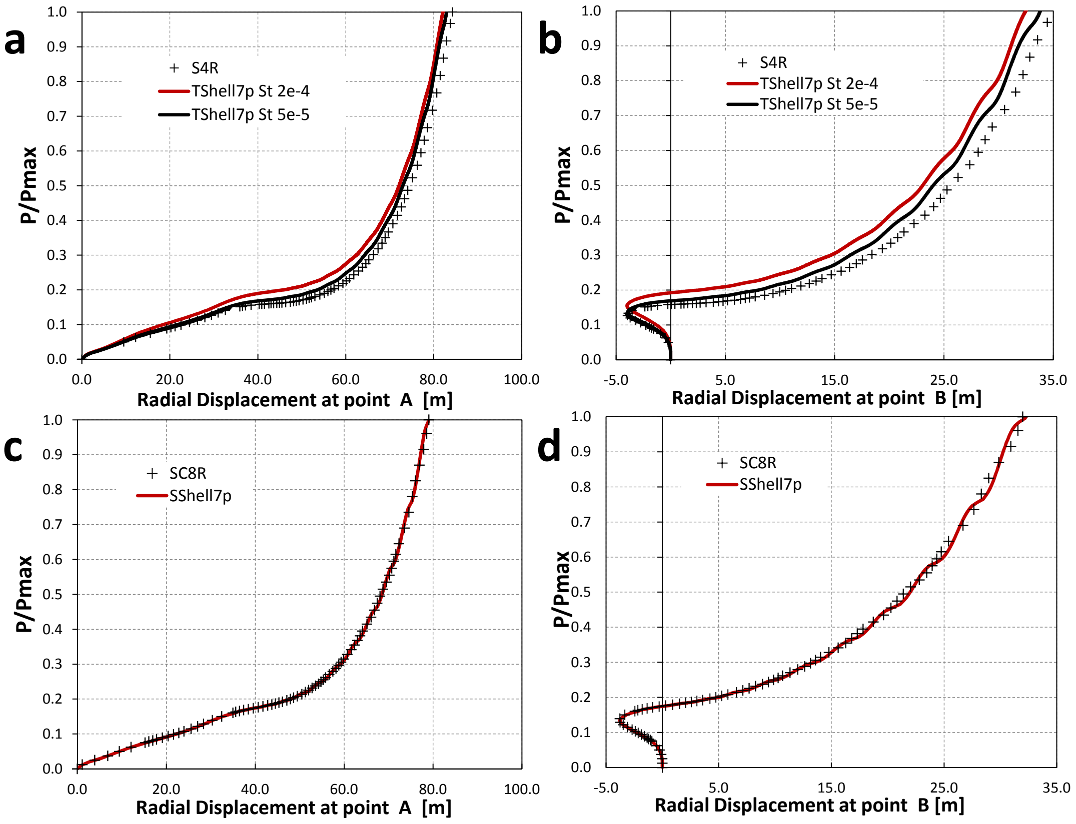

Figure 10: Pinched cylinder with end diaphragms. (a) Comparison of the evolution of the radial displacement at point A between the ABAQUS element S4R and the TShell7p element. (b) Comparison of the evolution of the radial displacement at point B between the ABAQUS element S4R and the TShell7p element. (c) Comparison of the evolution of the radial displacement at point A between the ABAQUS element SC8R and the SShell7p element. (d) Comparison of the evolution of the radial displacement at point B between the ABAQUS element SC8R and the SShell7p element.

Figs. 11.b and 11.c show the correlation between the present TShell7p and SShell7p elements with respect to the elements of ABAQUS S4R and SC8R, respectively, corresponding to the tip displacements along x-direction (u) and along the z-direction (w). In both graphs, an excellent agreement between the current shell elements and the reference results is observed. These simulations are computed using the ABAQUS/Standard solver employing a load control through the incremental Newton-Raphson scheme. The initial and maximum load step of 2.5% of the final load was applied. From the numerical perspective, a total of 202 iterations and 40 load increments for reaching the final load for the TShell7p element, whereas the SShell7p approach requires 141 iterations and 40 load increments. Note that for this second option and in line with previous considerations, minor problems in obtaining equilibrium solutions are found due to the fact that the nodal degrees of freedom have the same physical interpretation as that for the ABAQUS elements.

4.4.2 Application to layered CFRP composites

This example examines the extension of both TShell7p and SShell7p models to layered CFRP composites using a orthotropic law at lamina level. In line with the derivations outlined in Sect.3.3.1, ESL model is adopted. In particular, the laminated structures herewith analyzed consist of the stacking sequence $[45/\text{-}45]_S$, the zero-degree direction being coincident with to the x-axis (see the frame represented in Fig. 11.a). The orthotropic material properties selected for

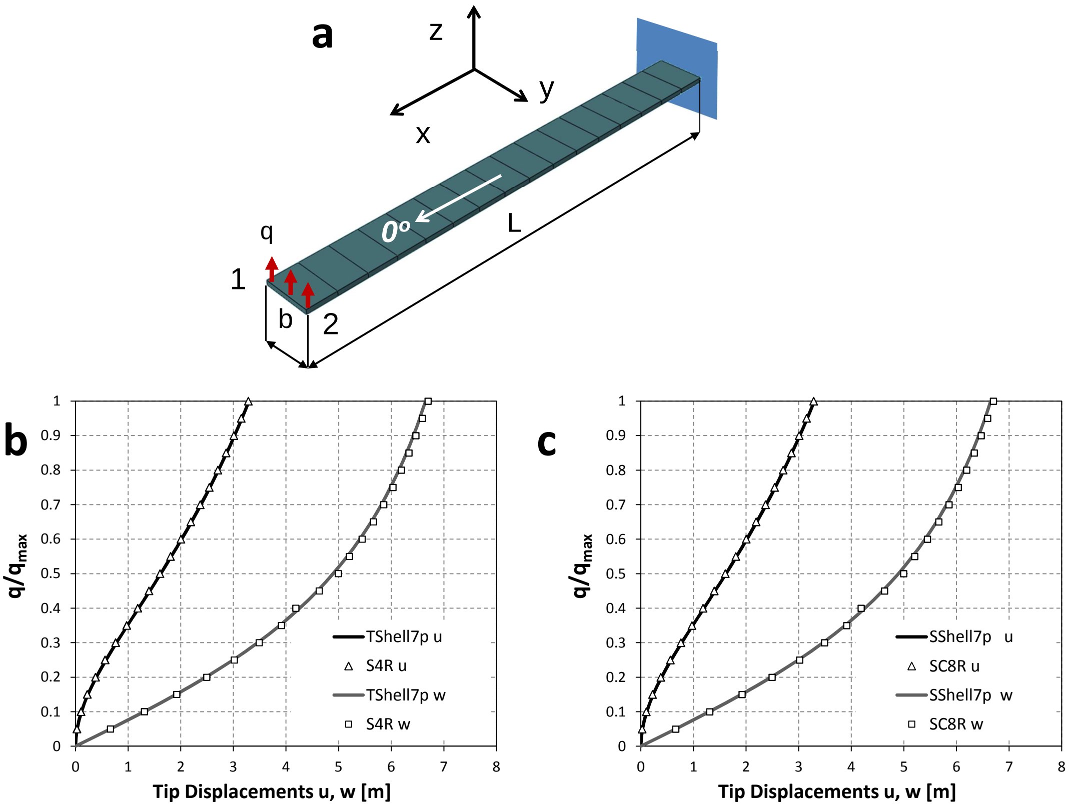

Figure 11: Cantilever beam subjected to distributed end load. (a) Geometry definition. (b) Load–displacement evolution curves for tip displacements: comparison between the TShell7p and S4R elements. (c) Load–displacement evolution curves for tip displacements: comparison between the SShell7p and SC8R elements.

this application are reported in Table 2 (which are comparable to the isotropic case analyzed above).

E_{11} (Pa)	$E_{22} = E_{33}$ (Pa)	$G_{12} = G_{13} = G_{23}$ (Pa)	$\nu_{12} = \nu_{13} = \nu_{23}$	h_L^* (m)
1.379×10^6	1.448×10^5	5.86×10^4	0.21	0.025

Table 2: Tip cantilever beam. Composite material data, h_L^* denoting the layer thickness.

Performing a similar analysis as that for the isotropic case, Fig. 12.a shows the tip displacements, in x and z directions, of the points 1 and 2 (Fig. 11.a), which are denoted by u and w, respectively. In this load-displacement evolution graph, the mechanical response of the structure using the aforementioned Mesh 8 for its discretization is compared with the solution provided by the ABAQUS element S4R, exhibiting an excellent agreement. Note that the TShell7p 7-parameter behaves slightly stiffer than the reduced integration element S4R. Similar conclusions can be attained for the case of the SShell7p element and its corresponding correlation with the element SC8R of ABAQUS, as is portrayed in Fig. 12.b.

4.4.3 Application to power-based FGMs

The nonlinear case of FGMs for the problem under analysis is considered for the same load and boundary conditions as described above. The material properties of the inhomogeneous beam vary continuously through the thickness direction. The metallic and ceramic constituents have the following properties: $E_m = 1.2 \times 10^6$ Pa, $E_c = 2.589 \times 10^6$ Pa are Young's moduli

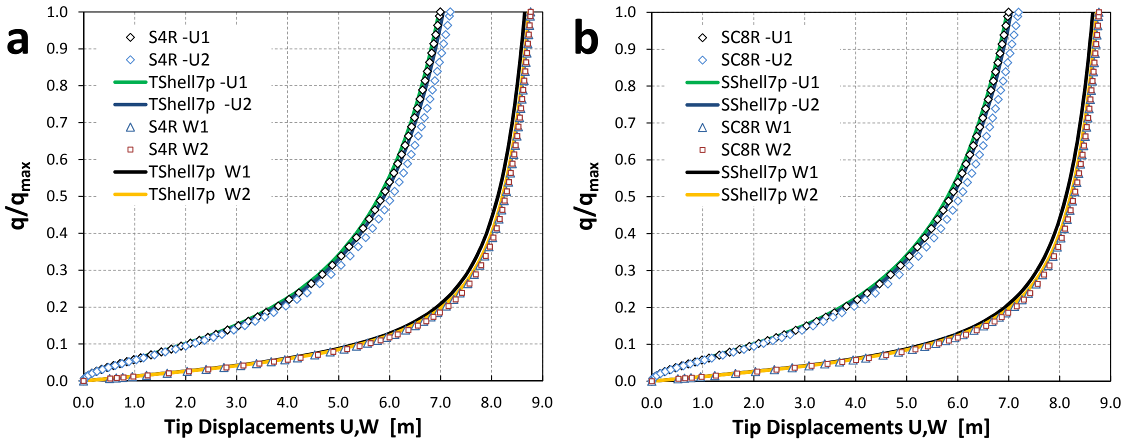

Figure 12: Cantilever beam subjected to distributed end load for layered composites with laminate $[45/\text{-}45]_S$. (a) Load–displacement evolution curves for tip displacements: comparison between the TShell7p and S4R elements. (b) Load–displacement evolution curves for tip displacements: comparison between the SShell7p and SC8R elements.

corresponding to the metallic and the ceramic constituents respectively, whereas $\nu = 0$ denotes the Poisson ratio that is assumed to be constant across the element thickness.

Fig. 13.a depicts the TShell7p results of the tip displacement in x and z directions vs. the external load applied for various volume fraction exponents n, which varies from the fully ceramic surface to the fully metallic surface. From the numerical perspective, the Newton-Raphson Method employed for the resolution process exhibits a good ratio of convergence for all the cases.

Analyzing the reported data, it is worth mentioning that, as was expected, the bending evolution curves of the FGMs are limited between the responses corresponding to the fully metallic and the fully ceramic cases. Similarly, the results referred to the SShell7p element using FGM law are depicted in Fig. 13.b. Coincident results are obtained for all the values of the exponent n in comparison with the TShell7p element.

4.5 Pullout of an open-ended cylindrical shell

This benchmark test deals with a cylindrical shell subjected to two opposite concentrated forces (Fig. 14.a, with radial displacements identified by W_A, U_B and U_c, for points A, B and C, respectively), whereby the cylindrical shell undergoes a combination of membrane and bending states [58].

The axial length of the cylinder is $L = 10.35$ m, with a radius $R = 4.953$ m and a shell thickness of $h = 0.094$ m. In the case of isotropic constitutive law, the material properties are: Young's Modulus $E = 10.5 \times 10^6$ Pa, and Poisson ratio $\nu = 0.3125$. The pair of external concentrated loads each has a value of 40 kN each of them. Regarding the boundary conditions, the structure has free axial edges and only the symmetry conditions are imposed, therein one eighth of the cylinder is modeled.

The cylinder is discretized using a mesh density of 16 × 24 elements (Fig. 14.a), in order to be compared with the results reported in [58]. As was considered in previous applications, the two 7-parameter shell elements examined in this work are applied to this problem, i.e. the TShell7p and the SShell7p elements.

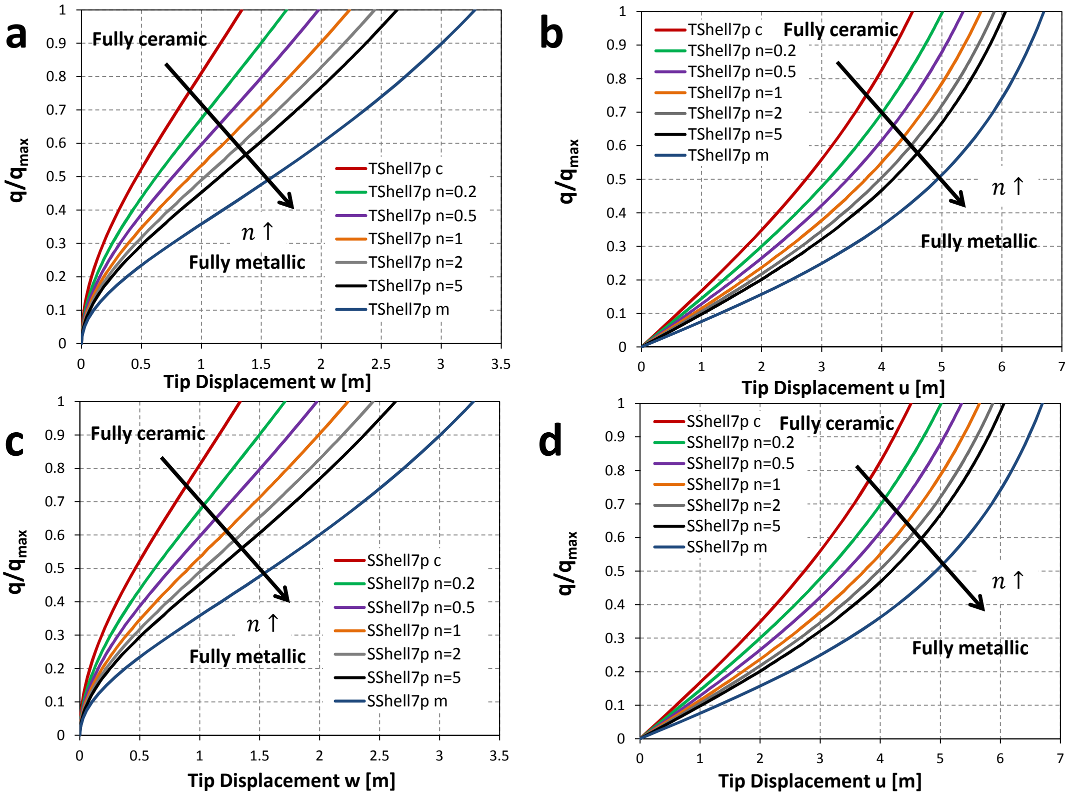

Figure 13: Power-based FG tip cantilever beam subjected to end forces. (a) Load–displacement evolution curves for the TShell7p formulation. (b) Load–displacement evolution curves for the SShell7p formulation.

4.5.1 Isotropic material law

Simulations are conducted using either load control or displacement control schemes which lead to the same quantitative results. Fig.14.b depicts the final deformed shape for the current application using the TShell7p element with isotropic material law. Converged solutions are compared with the results by modeling with standard ABAQUS elements S4R, for the case of the TShell7p element, and SC8R for the SShell7p element.

The simulations are carried out through the use of the standard Newton-Raphson method, using loading (with and without the ABAQUS's parameter `*stabilize`, being the later option labelled as St) and displacement control procedures (labeled as Ucont), whose main characteristics are detailed in Table 3. The initial and the maximum load step applied was equal to 1% of the final load for both procedures.

Label	$[\frac{\Delta p}{p_{final}}]_{min}$	$[\frac{\Delta p}{p_{final}}]_{max}$	$[\frac{\Delta p_{max}}{p_{final}}]$	N_{inc}	N_{iter}
TShell7p	1×10^{-8}	0.01	0.516	70	533
TShell7p St	6.3×10^{-6}	0.01	1	1358	5987
TShell7p Ucont	0.00625	0.01	1	42	186
SShell7p	6.59×10^{-5}	0.01	1	118	300
SShell7p Ucont	0.01	0.01	1	100	373

Table 3: Pullout of an open-ended cylindrical shell: summary of the solution processes, TShell7p and SShell7p elements. $[\frac{\Delta p}{p_{final}}]_{min}$ is the minimum load increment size; $[\frac{\Delta p}{p_{final}}]_{min}$ is the maximum load increment size; $[\frac{\Delta p_{max}}{p_{final}}]$ denotes the final load reached; N_{inc} indicates the total number of load increments; and N_{iter} denotes the number of iterations for the complete solution process

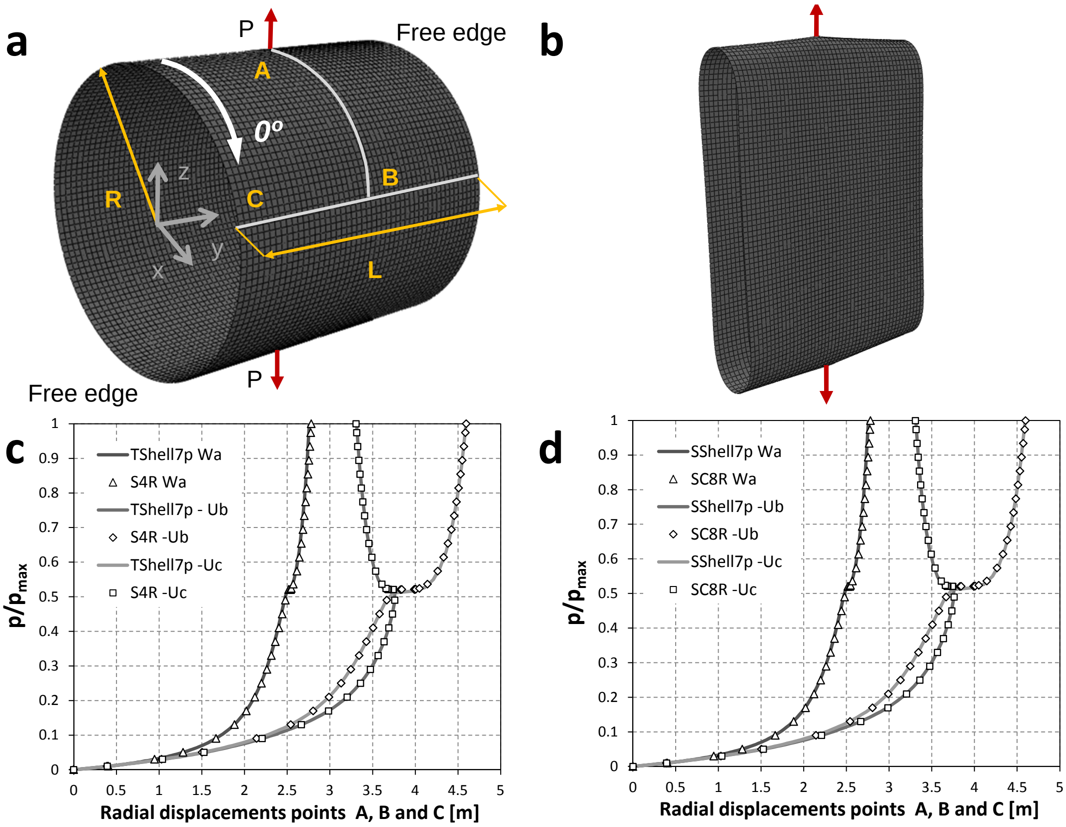

Figure 14: Pullout of an open-ended cylindrical shell. (a) Geometric and boundary conditions. (b) Final deformed shape TShell7p element. (c) Comparison of the load-deflection curves between the ABAQUS element S4R and the TShell7p element. (d) Comparison of the load-deflection curves between the ABAQUS element SC8R and the SShell7p element.

First, with reference to the TShell7p, Table 3, it can be observed that employing the load control procedure without any additional features, the numerical simulation only reached 51.6% of the final load. However, by including the `*stabilize` option, the analysis is finished successfully (1358 load increments and 5987 equilibrium iterations being required), and provides satisfactory results in comparison with the reference solutions provided by the ABAQUS element S4R, see Fig.14.c. On the other hand, using a displacement control scheme, it can be appreciated how the simulations require a reduced number of step increments and iterations (42 load increments and 186 equilibrium iterations), and therefore the solutions process seems to achieve each of the equilibrium states along the load path with less computational efforts, see Table 3.

Second, regarding the numerical results obtained for the SShell7p element, note that significantly less convergence problems appeared during the analysis (see Table 3) as well as excellent agreement with the ABAQUS element SC8R is obtained for loading and displacement control procedures, see Fig.14.d.

4.5.2 Application to layered CFRP composites

The analysis of the problem under consideration is also performed using composite unidirectional laminates. In line with the previous applications, the present implementation is validated through performing a comparison of the results referred to the three-dimensional and the solid shell 7-parameter shell elements are compared with those obtained using ABAQUS elements.

The material data are reported in Table 4. In a similar way as in the previous section, and as a consequence of the existence of geometric symmetry, only one octant of the cylinder is considered in the analyses. Therefore, laminates that satisfy these symmetry conditions are tested, namely [0/90/0] and [90/0/90] orientations, where the fiber direction is identified with the circumferential axis of the cylinder.

The problem is modeled using a regular mesh of 16×24 elements. The load is applied using an initial and maximum step size of 1% of the final load $P = 30$ kN, employing a nonlinear load control scheme.

E_{11} (Pa)	$E_{22} = E_{33}$ (Pa)	$G_{12} = G_{13} = G_{23}$ (Pa)	$\nu_{12} = \nu_{13} = \nu_{23}$	h_L^* (m)
3.11×10^7	1.06×10^7	2.9×10^6	0.4	0.033

Table 4: Pullout of an open-ended cylindrical shell. Composite material data, h_L^* denoting the layer thickness

Figs. 15.a and 15.b depict the radial displacements for the point A, B and C (14.a) for the TShell7p element for both laminate configurations. Comparisons of the present results with the response obtained through the use of the ABAQUS element S4R are in close agreement, with the TShell7p elements behaving slightly stiffer especially for the radial displacement of the point A for the [90/0/90] laminate. From the computational standpoint, a loading control scheme is employed for the nonlinear process, where the initial and the maximum step size being equal to 1% of the maximum load. The resolution procedure found significant convergence difficulties in achieving equilibrium solutions, resulting in the step size being decreased to 1×10^{-8} of the total load for the laminate [0/90/0], whereas these absence numerical difficulties referred to the solution process are not found for the laminate [90/0/90].

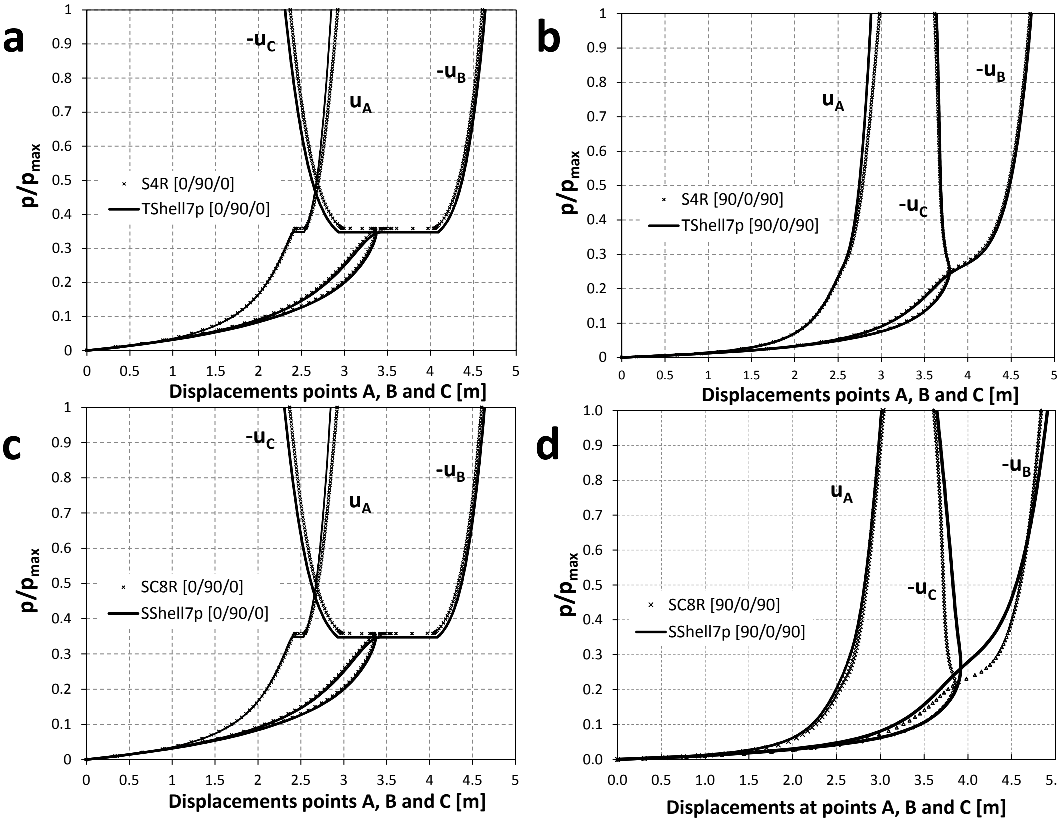

Figure 15: Pullout of an open-ended layered cylindrical shell. Load-deflection curve using the TShell7p element in comparison with the ABAQUS element S4R. (a) Laminate [0/90/0]. (b) Laminate [90/0/90]. Load-deflection curve using the SShell7p element in comparison with the ABAQUS element SC8R. (c) Laminate [0/90/0]. (d) Laminate [90/0/90].

The results corresponding to the SShell7p element in comparison with the elements SC8R of ABAQUS are shown in Figs. 15.c and 15.d, where a good level of agreement can be observed. Note for the laminate [90/0/90], mid discrepancies are identified, especially for the evolutions of the points B and C. In this regard, it is worth mentioning that the resolution process encounters strong difficulties in achieving equilibrium solutions for the laminate [0/90/0], which requires the use of the `*stabilize` option with a damping factor equal to 2×10^{-4} for this specific configuration. Therefore, the incorporation of such artificial damping might be responsible for such discrepancies in comparison with the solution of predicted by the elements of ABAQUS.

4.5.3 Application to power-based FGMs

For comparison purposes, the current cantivelever beam application is extended to FGMs. The material properties are coincident with those reported in Sect.4.4.3, and imposing a pair external point loads equal to 500 kN. The material gradation is again assumed over the thickness direction of the shell. In Fig. 16 the obtained numerical results at the points A and B for the TShell7p element are compared with those presented in [39] (corresponding to the SShell7p case) which showed an excellent agreement with the reference data in [51] for the same application. In these graphs, an very good correlation between TShell7p and SShell7p results can be observed. Note also that from the qualitative point of view, as expected, the evolutions of the power-based FGMs lie again within between the fully ceramic and the fully metallic configurations.

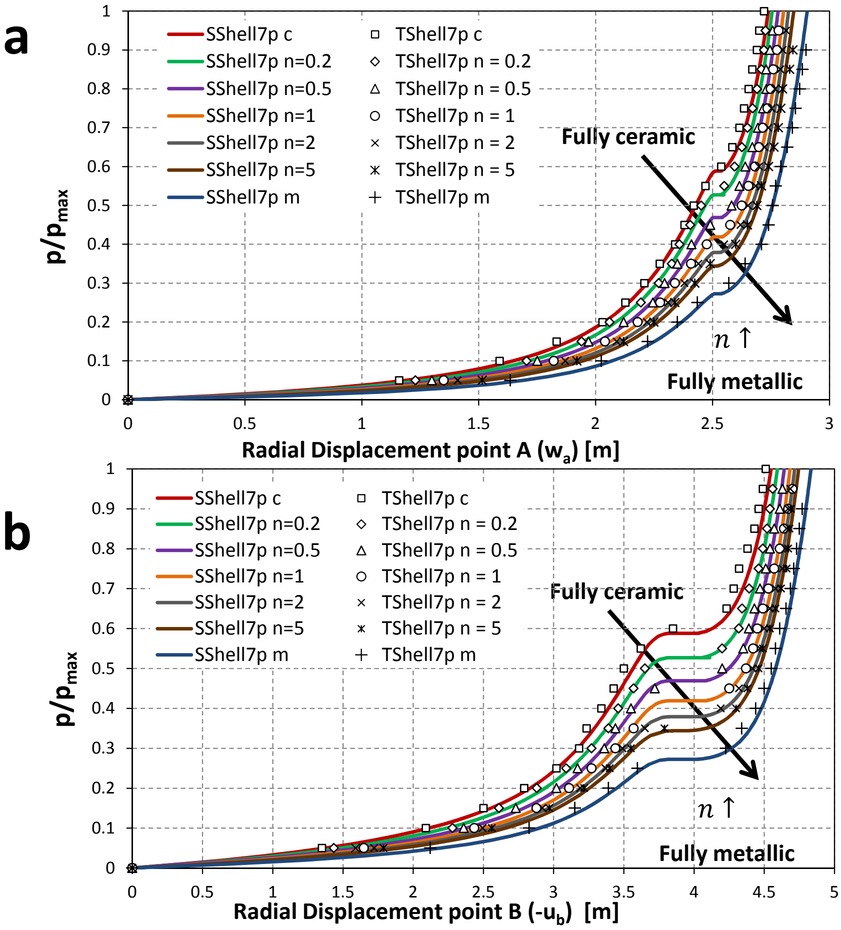

Figure 16: Power-based FG pullout of an open-ended cylindrical shell. Radial deflection curves at the points A and B: comparison between TShell7p and SShell7p results.

5 Conclusions

In this paper, the consistent extensions of the 7p shell model for its application to layered CFRP and functionally graded power-based composite structures have been developed. In particular, two different kinematic parametrizations were employed and thoroughly described, namely the three-dimensional shell formulation (surface-based FE meshes), and the so-called solid shell approach (solid-based FE meshes). Both models have been implemented into the FE code ABAQUS through the user-defined capability `UEL`. Locking pathologies have been remedied through the combined use of the Enhanced Assumed Strain (EAS) and the Assumed Natural Strain (ANS) methods.

The applicability of the current developments has been demonstrated via an extensive benchmark data base, whereby the numerical results obtained using both elements here proposed have been compared to the alternative shell elements, either implemented into the software ABAQUS or developed by other authors. The success of the computations can be attested from the overall results obtained in geometrically linear and nonlinear ranges, and for the constitutive laws considered: homogeneous (isotropic material law) and composite (ESL approach and Functionally Graded Materials) materials.

From the computational point of view, the so-called three-dimensional 7-p formulation encountered severe converging difficulties in achieving equilibrium solutions. This aspect was attributed due to the fact that in such shell parametrization, the nodal degrees of freedom 4, 5 and 6 contains the kinematic information corresponding to the difference vector $\mathbf{w}$ instead of rotations as in standard shell elements. Therefore, in some of the cases, the inclusion of the ABAQUS's `*stabilize` option in a Newton-Rapshon scheme as well as arc-length procedures were required in order to reach the final load applied, conforming with the residual tolerance criteria of ABAQUS. On the other side, the solid shell 7p formulation presented less numerical difficulties in achieving equilibrium solutions, since the nodal degrees of freedom have the same significance as the elements of ABAQUS (coinciding with those referred to standard brick elements).

Finally, further research activities might regard the incorporation of computational fracture modeling capabilities as those developed by the authors in [41, 43], among others.

Acknowledgments

JR appreciates the support of the projects funded by the Spanish Ministry of Economy and Competitiveness (Projects MAT2015-71036-P and MAT2015-71309-P) and the Andalusian Government (Projects of Excellence No. TEP-7093 and P12-TEP-1050). MP and JR would like to acknowledge support from the European Research Council to the ERC Starting Grant Multi-field and multi-scale Computational Approach to Design and Durability of PhotoVoltaic ModulesCA2PVM, under the European Unions Seventh Framework Programme (FP/2007-2013)/ERC Grant Agreement no. 306622.

A Definition of the shell director vector for the three dimensional shell model

The definition of the shell director vector is inherently present within the discretization procedure of an arbitrary shell body using surface-based meshes for FE analyses. This vector provides the thickness direction of the shell, which is currently of issue of notable importance to represent the ut-of-plane behavior, and it contains the information about the direction of the pre-integration of the material law.

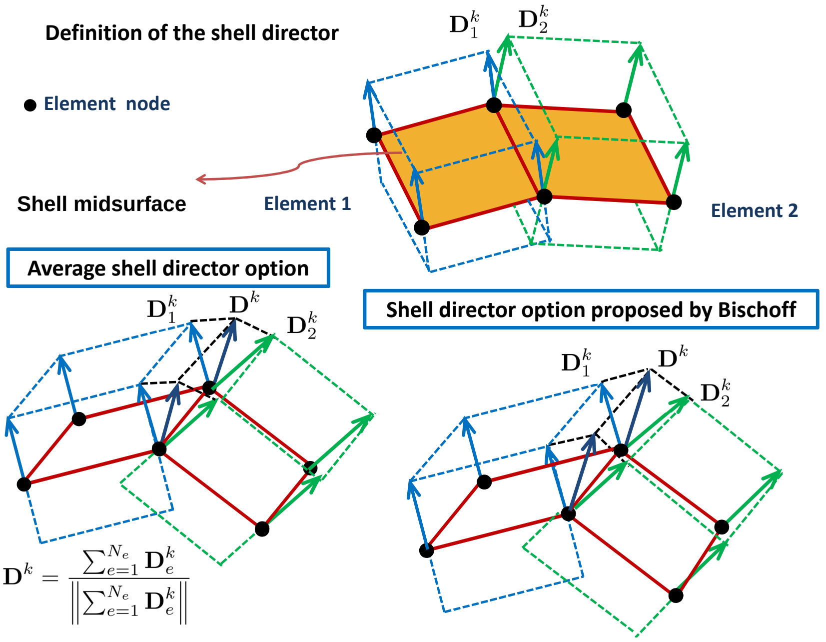

Figure A.1: Definition of the shell director vector for the three dimensional shell parametrization: standard average procedure and spatial intersections of the actual three-dimensional geometries as proposed in [55].

The natural choice of computing the shell director common to adjacent elements is due to an averaging-type procedure, and hence, the inter-element continuity of the shell normal is ensured as being

$$\mathbf{D}^k = \frac{\sum_{e=1}^{N_e} \mathbf{D}_e^k}{\left\| \sum_{e=1}^{N_e} \mathbf{D}_e^k \right\|} \tag{A.1}$$

where $\mathbf{D}_e^k$ denotes the shell director of the element e at the node k. This procedure violates the condition of orthogonality with respect to the shell midsurface in addition to the material overlapping. This is usually minimized by shell refinement, not representing a relevant problem, although it is more pronounced at corners locations.

However, for the particular case of the three-dimensional shell parametrization, the standard averaging procedure leads to artificial necking effects, making the structure more flexible at these regions [55, 54]), see to the left of Fig A.1. Therefore, in the present formulation, the shell director is recommended to be defined according to Bischoff [55], which is based on the spatial intersections of the actual three-dimensional geometries, see to the right of Fig. A.1.

Moreover, as was pointed out in Bischoff et al. [54], this definition of the common director vector between adjacent elements violates the orthogonality condition to the shell midsurface. However, this aspect has a very minor role and vanishes with the mesh refinement. In view of these arguments, the current option becomes especially suitable in the case of dealing with smooth shells, whereas for problems involving kinks and intersections, the definition of individual shell directors together with drilling rotations can be assumed as the better choice [54].

Finally, note that the computation of the nodal director vector requires the use of an auxiliary script as was described in [38]. This fact can be as a shortcoming of the current parametrization since this average procedure specifically depends on the mesh characteristics.

B Computation of the compatible displacements-strain operators

This section presents the derivation of the compatible displacements-strain operators corresponding to the three dimensional shell and the solid shell parametrizations outlined in Sects. 2.2 and 2.3, respectively.

With respect to the three dimensional shell parametrization using a 4-node element formulation, the B-operator in Eq.(34) adopts the form:

$$\delta \mathbf{E}^u \approx \mathbf{B}(\mathbf{d})\delta\mathbf{d} = \sum_{I=1}^{4} \mathbf{B}^I \delta\mathbf{d}^I = \sum_{I=1}^{4} \begin{bmatrix} \mathbf{B}_v^I & \mathbf{B}_w^I \end{bmatrix} \begin{bmatrix} \delta\mathbf{v}^I \\ \delta\mathbf{w}^I \end{bmatrix} \tag{B.2}$$

where the displacement vectors $\mathbf{v}^I$ and $\mathbf{w}^I$ are the misurface and difference displacement vectors of the node I. Thus, the B-operator at nodal level is given by

$$\mathbf{B}^I = \begin{bmatrix} \mathbf{B}_v^I & \mathbf{B}_w^I \end{bmatrix} = \begin{bmatrix} N^I_{,\xi^1}\mathbf{a}_1 & \mathbf{0}_{1\times 3} \\ N^I_{,\xi^1}\mathbf{a}_2 + N^I_{,\xi^2}\mathbf{a}_1 & \mathbf{0}_{1\times 3} \\ N^I_{,\xi^1}\mathbf{a}_3 & N^I\mathbf{a}_1 \\ N^I_{,\xi^2}\mathbf{a}_2 & \mathbf{0}_{1\times 3} \\ N^I_{,\xi^2}\mathbf{a}_3 & N^I\mathbf{a}_2 \\ \mathbf{0}_{1\times 3} & N^I\mathbf{a}_3 \\ N^I_{,\xi^1}\mathbf{a}_{3,\xi^1} & N^I_{,\xi^1}\mathbf{a}_1 + N^I_{,\xi^2}\mathbf{a}_2 \\ N^I_{,\xi^1}\mathbf{a}_{3,\xi^2} + N^I_{,\xi^2}\mathbf{a}_{3,\xi^1} & N^I\mathbf{a}_{3,\xi^1} + N^I_{,\xi^1}\mathbf{a}_3 \\ \mathbf{0}_{1\times 3} & N^I_{,\xi^2}\mathbf{a}_2 \\ N^I_{,\xi^2}\mathbf{a}_{3,\xi^2} & N^I\mathbf{a}_{3,\xi^2} + N^I_{,\xi^2}\mathbf{a}_3 \\ \mathbf{0}_{1\times 3} & N^I_{,\xi^2}\mathbf{a}_2 \\ \mathbf{0}_{1\times 3} & \mathbf{0}_{1\times 3} \end{bmatrix}, \tag{B.3}$$

where $\mathbf{0}_{1\times 3}$ is the null vector of dimension 1×3; and $\mathbf{B}_v^I$ and $\mathbf{B}_w^I$ stand for the parts of the B-operator arranged in column form that are respectively referred to the displacement vectors of the shell midsurface $\mathbf{v}$ and the director vector $\mathbf{w}$.

In a similar manner, the discrete version of the B-operator corresponding to the solid shell parametrization of the 7-p shell model reads

$$\delta \mathbf{E}^u \approx \mathbf{B}(\mathbf{d})\delta\mathbf{d} = \sum_{I=1}^{4} \mathbf{B}^I \delta\mathbf{d}^I = \sum_{I=1}^{4} \begin{bmatrix} \mathbf{B}_t^I & \mathbf{B}_b^I \end{bmatrix} \begin{bmatrix} \delta\mathbf{d}_t^I \\ \delta\mathbf{d}_b^I \end{bmatrix} \tag{B.4}$$

where $\mathbf{B}_b^I$ and $\mathbf{B}_t^I$ denote the terms associated with the bottom and top nodal displacements of the solid shell element using an 8-node element, respectively, and $\mathbf{d}_b^I$ and $\mathbf{d}_t^I$ denotes the corresponding bottom and top displacement vectors for the corner point I of the element. The compact form of the B-operator renders

$$
\mathbf{B}^I = \begin{bmatrix}
\frac{1}{2}N^I_{,\xi^1}\mathbf{a}_1 & \frac{1}{2}N^I_{,\xi^1}\mathbf{a}_1 \\
\frac{1}{2}N^I_{,\xi^2}\mathbf{a}_1 + \frac{1}{2}N^I_{,\xi^1}\mathbf{a}_2 & \frac{1}{2}N^I_{,\xi^2}\mathbf{a}_1 + \frac{1}{2}N^I_{,\xi^1}\mathbf{a}_2 \\
\frac{1}{2}N^I_{,\xi^1}\mathbf{a}_3 + \frac{1}{2}N^I\mathbf{a}_1 & \frac{1}{2}N^I_{,\xi^1}\mathbf{a}_3 - \frac{1}{2}N^I\mathbf{a}_1 \\
\frac{1}{2}N^I_{,\xi^2}\mathbf{a}_2 & \frac{1}{2}N^I_{,\xi^2}\mathbf{a}_2 \\
\frac{1}{2}N^I_{,\xi^2}\mathbf{a}_3 + \frac{1}{2}N^I\mathbf{a}_2 & \frac{1}{2}N^I_{,\xi^2}\mathbf{a}_3 - \frac{1}{2}N^I\mathbf{a}_2 \\
\frac{1}{2}N^I\mathbf{a}_3 & -\frac{1}{2}N^I\mathbf{a}_3 \\
\frac{1}{2}N^I_{,\xi^1}\mathbf{a}_{3,\xi^1} + \frac{1}{2}N^I_{,\xi^1}\mathbf{a}_1 & \frac{1}{2}N^I_{,\xi^1}\mathbf{a}_{3,\xi^1} - \frac{1}{2}N^I_{,\xi^1}\mathbf{a}_1 \\
\frac{1}{2}N^I_{,\xi^1}\mathbf{a}_{3,\xi^2} + \frac{1}{2}N^I_{,\xi^2}\mathbf{a}_1 + \frac{1}{2}N^I_{,\xi^2}\mathbf{a}_{3,\xi^1} + \frac{1}{2}N^I_{,\xi^1}\mathbf{a}_2 & \frac{1}{2}N^I_{,\xi^1}\mathbf{a}_{3,\xi^2} - \frac{1}{2}N^I_{,\xi^2}\mathbf{a}_1 + \frac{1}{2}N^I_{,\xi^2}\mathbf{a}_{3,\xi^1} - \frac{1}{2}N^I_{,\xi^1}\mathbf{a}_2 \\
\frac{1}{2}N^I_{,\xi^1}\mathbf{a}_{3,\xi^1} + \frac{1}{2}N^I\mathbf{a}_3 & -\frac{1}{2}N^I_{,\xi^1}\mathbf{a}_{3,\xi^1} - \frac{1}{2}N^I\mathbf{a}_3 \\
\frac{1}{2}N^I_{,\xi^2}\mathbf{a}_{3,\xi^2} + \frac{1}{2}N^I_{,\xi^2}\mathbf{a}_2 & \frac{1}{2}N^I_{,\xi^2}\mathbf{a}_{3,\xi^2} - \frac{1}{2}N^I_{,\xi^2}\mathbf{a}_2 \\
N^I_{,\xi^2}\mathbf{a}_{3,\xi^2} + \frac{1}{2}N^I_{,\xi^2}\mathbf{a}_{3,\xi^2} + \frac{1}{2}N^I_{,\xi^2}\mathbf{a}_3 & N^I_{,\xi^2}\mathbf{a}_2 - \frac{1}{2}N^I_{,\xi^2}\mathbf{a}_{3,\xi^2} - \frac{1}{2}N^I_{,\xi^2}\mathbf{a}_3 \\
\mathbf{0}_{1\times 3} & \mathbf{0}_{1\times 3}
\end{bmatrix}. \tag{B.5}
$$

C The ANS method

The ANS method in shells is a collocation technique which is used in this formulation for the alleviation of two locking pathologies: (i) the transverse shear locking [22], and (ii) the trapezoidal locking [23]. This method is implemented in combination to the EAS method, so that locking free shell elements can be derived.

For the alleviation of the so-called transverse shear locking, the interpolation of the (compatible) constant transverse shear components p_{13} and p_{23} are evaluated at the collocation points A, B, C and D (Fig. C.2) with: $\boldsymbol{\xi}_A = (0,-1,0)$, $\boldsymbol{\xi}_B = (1,0,0)$, $\boldsymbol{\xi}_C = (0,1,0)$ and $\boldsymbol{\xi}_D = (-1,0,0)$. The modified interpolation of the constant transverse shear components read

$$
\begin{bmatrix} p_{13}^{ANS} \\ p_{23}^{ANS} \end{bmatrix} = \begin{bmatrix} (1-\xi^2)p_{13}(\boldsymbol{\xi}_A) + (1+\xi^2)p_{13}(\boldsymbol{\xi}_C) \\ (1+\xi^1)p_{23}(\boldsymbol{\xi}_B) + (1-\xi^1)p_{23}(\boldsymbol{\xi}_D) \end{bmatrix} \tag{C.6}
$$

Similarly, for the treatment of the trapezoidal locking, the constant transverse normal strain component are evaluated at the collocation points M, N, O and P (Fig. C.2), with: $\boldsymbol{\xi}_M = (-1,-1,0)$, $\boldsymbol{\xi}_N = (1,-1,0)$, $\boldsymbol{\xi}_O = (1,1,0)$ and $\boldsymbol{\xi}_P = (-1,1,0)$. Then, the modified approximation of p_{33} renders

$$
p_{33}^{ANS} = \sum_{m=1}^{4} N^m(\xi^1,\xi^2)p_{33}; \quad N^m(\xi^1,\xi^2) = \frac{1}{4}\left(1+\xi^1_m\xi^1\right)\left(1+\xi^2_m\xi^2\right), \quad \text{with } \ m = M,N,O,P \tag{C.7}
$$

References

References

[1] E. Carrera (2001) Developments, ideas, and evaluations based upon Reissner's Mixed Variational Theorem in the modeling of multilayered plates and shells. Applied Mechanics Reviews, 54:301–328.

[2] E. Carrera, M. Cinefra, A. Lamberti, M. Petrolo (2015) Results on best theories for metallic and laminated shells including Layer-Wise models. Compos Struct 126:285–298.

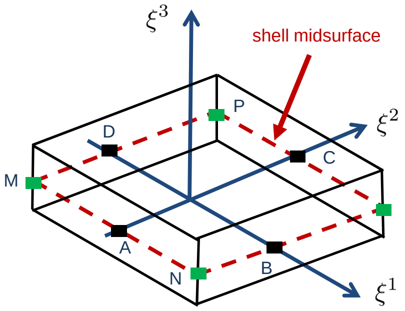

Figure C.2: Collocation points of the linear 7-parameter shell element for the alleviation of the transverse shear and trapezoidal locking through the ANS method.

[3] J.D. Rodrigues, C.C. Roque, A.J.M. Ferreira, E. Carrera, M. Cinefra (2011) RBF-FD collocation and a unified formulation for bending, vibration and buckling analysis of laminated plates, according to Murakamis zig-zag theory. Composite Structures 93:1613–1620.

[4] E. Carrera (2002) Theories and Finite Elements for Multilayered Anisotropic, Composite Plates and Shells. Archives of Computational Methods in Engineering, 9:87–140.

[5] M.B. Dehkordi, S.M.R. Khalili, E. Carrera (2016) Non-linear transient dynamic analysis of sandwich plate with composite face-sheets embedded with shape memory alloy wires and flexible core-based on the mixed LW (layer-wise)/ESL (equivalent single layer) models Compos B Eng, 87:59–74.

[6] A.J.M. Ferreira, A.L. Arajo, A.M.A. Neves, J.D. Rodrigues, E. Carrera, M. Cinefra, C.M. Mota Soares (2013) A finite element model using a unified formulation for the analysis of viscoelastic sandwich laminates. Compos Part B, 203 (45):1258–1264.

[7] D.H. Robbins Jr, J.N. Reddy (1993) Modeling of thick composites using a layer-wise theory. Int J Numer Methods Engm, 36:655–677.

[8] J.N. Reddy (1997) Mechanics of Laminated Composite Plates, Theory and Analysis, CRC Press, ISBN 9780849315923.

[9] C.H. Thai, A.J.M. Ferreira, E. Carrera, H. Nguyen-Xuan (2013) Isogeometric analysis of laminated composite and sandwich plates using a layerwise deformation theory. Compos Struct 104:196–214.

[10] F. Tornabene (2016) General higher-order layer-wise theory for free vibrations of doubly-curved laminated composite shells and panels Mech Adv Mater Struct, 23:1046–1067.

[11] M. Cinefra, E. Carrera, S. Valvano (2015) Variable Kinematic Shell Elements for the Analysis of Electro-Mechanical Problems. Mechanics of Advanced Materials and Structures, 22(1-2)77–106.

[12] A.J.M. Ferreira, C.M. Roque, E. Carrera, M. Cinefra, O. Polit (2013) Bending and Vibration of Laminated Plates by a Layerwise Formulation and Collocation with Radial Basis Functions, Mechanics of Advanced Materials and Structures 20:624–637.

[13] R.A. Arciniega, J.N. Reddy (2007) Tensor–based finite element formulation for geometrically nonlinear analysis of shell structures. Computer Methods in Applied Mechanics and Engineering, 196:1048-1073.

[14] Y. Başar, M. Itskov, A. Eckstein, (2000) Composite laminates: nonlinear interlaminar stress analysis by multi–layer shell elements. Computer Methods in Applied Mechanics and Engineering, 185:367–397.

[15] M. Bischoff, E. Ramm (1997) Shear deformable shell elements for large strains and rotations. International Journal for Numerical Methods in Engineering, 40:4427–4449.

[16] J.C. Simo, M.S. Rifai, D.D. Fox (1990) On a stress resultant geometrically exact shell model. Part IV: Variable thickness shells with through-the-thickness stretching. Computer Methods in Applied Mechanics and Engineering, 81:91–126.

[17] J.L. Ericksen, C. Truesdell (1958) Exact theory of stress and strain in rods and shells. Archive for Rational Mechanics and Analysis, 1:295–323.

[18] P.M. Naghdi (1972) The Theory of Shells, in: Handbuch der Physik, Vol. VI/2, Springer, Berlin.

[19] Bischoff M, Ramm E. (2000) On the Physical Significance of Higher Order Kinematic and Static Variables in a Three–Dimensional Shell Formulation. International Journal of Solids and Structures, 37:6933-6960.

[20] H. Parisch (1995) A continuum-based shell theory for non-linear applications. International Journal for Numerical Methods in Engineering, 38:1855–1883.

[21] M.G. Rivera, J.N. Reddy, M. Amabili (2016) A new twelve-parameter spectral/hp shell finite element for large deformation analysis of composite shells. Composite Structures, 151:183–196.

[22] K.J. Bathe, E.N. Dvorkin (1985) A four-node plate bending element based on Mindlin/Reissner plate theory and a mixed interpolation, International Journal for Numerical Methods in Engineering, 21:367–383.

[23] P. Betsch, F. Gruttmann, E. Stein (1996) A 4-node finite shell element for the implementation of general hyperelastic 3D-elasticity at finite strains. Computer Methods in Applied Mechanics and Engineering, 130:57–79.

[24] S. Glaser, F. Armero (1997) On the formulation of enhanced strain finite elements in finite deformations. Engineering Computations, 14:759-791.

[25] J.C. Simo, F. Armero (1992) Geometrically nonlinear enhanced strain mixed methods and the method of incompatible modes. International Journal for Numerical Methods in Engineering, 33:1413–1449.

[26] L. Vu-Quoc, X.G. Tan (2003) Optimal solid shells for non-linear analyses of multilayer composites. I. Statics. Computer Methods in Applied Mechanics and Engineering, 192:975–1016.

[27] P. Wriggers, S. Reese (1996) A note on enhanced strain methods for large deformations. Computer Methods in Applied Mechanics and Engineering, 135:201-209.

[28] F. Gruttmann, W. Wagner (2006) Structural analysis of composite laminates using a mixed hybrid shell element. Computational Mechanics, 37:479–497.

[29] E. Kasper, R.L. Taylor (2000) A mixed–enhanced strain method. Part I: geometrically linear problems. Computers and Structures, 75:237-250.

[30] E. Kasper, R.L. Taylor (2000) A mixed–enhanced strain method. Part II: geometrically nonlinear problems. Computers and Structures, 75:251-260.

[31] S. Klinkel, F. Gruttmann, W. Wagner (2006) A robust non-linear solid shell element based on a mixed variational formulation. Computer Methods in Applied Mechanics and Engineering, 195:179–201.

[32] L. Vu-Quoc, X. Tan (2013) Efficient hybrid-EAS solid element for accurate stress prediction in thick laminated beams, plates, and shells. Computer Methods in Applied Mechanics and Engineering, 253:337–355.

[33] M. Schwarze, S. Reese (2009) A reduced integration solid-shell element based on the EAS and the ANS conceptgeometrically linear problems. International Journal for Numerical Methods in Engineering, 80:1322–1355.

[34] S. Reese (2007) A large deformation solid-shell concept based on reduced integration with hourglass stabilization. International Journal for Numerical Methods in Engineering, 69:1671–1716.

[35] M. Braun, M. Bischoff, E. Ramm (1994) Nonlinear Shell Formulations for Complete Three–Dimensional Constitutive Laws Including Composites and Laminates. Computational Mechanics, 15:1–18.

[36] N. Büchter, E. Ramm (1992) Shell theory versus degeneartion- a comparison in large rotation finite element analysis. International Journal for Numerical Methods in Engineering, 34:39–59.

[37] N. Büchter, E. Ramm, D. Roehl (1994) Three-dimensional extension of nonlinear shell formulation based on the enhanced assumed strain concept. International Journal for Numerical Methods in Engineering, 37:2551–2568.

[38] J. Reinoso, A. Blázquez (2016) Application and finite element implementation of 7-parameter shell element for geometrically nonlinear analysis of layered CFRP composites. Composite Structures 139:263–276.

[39] J. Reinoso, A. Blázquez (2016) Geometrically nonlinear analysis of functionally graded power-based and carbon nanotubes reinforced composites using a fully integrated solid shell element. Composite Structures 152:277–294.

[40] J. Reinoso, M. Paggi, P. Areias (2016) A finite element framework for the interplay between delamination and buckling of rubber-like bi-material systems and stretchable electronics. Journal of the European Ceramic Society, 36(9):2371–2382.

[41] J. Reinoso, M. Paggi, C. Linder (2017) Phase field modeling of brittle fracture for enhanced assumed strain shells at large deformations: formulation and finite element implementation. Computational Mechanics 59 (6), 981–1001.

[42] P.R. Budarapu, J. Reinoso, M. Paggi (2017) Concurrently coupled solid shell based adaptive multiscale method for fracture. Computer Methods in Applied Mechanics and Engineering 319, 338–365.

[43] J. Reinoso, G. Catalanotti, A. Blázquez, P. Areias, P.P. Camanho, F. París, (2017) A consistent anisotropic damage model for laminated fiber-reinforced composites using the 3D-version of the Puck failure criterion, International Journal of Solids and Structures, in press.

[44] J. Reinoso, M. Paggi, A. Blázquez (2017) A modeling framework for the analysis of instabilities and delamination in composite shells. Mathematical Methods and Models in Composites (2nd extended edition). Imperial College Press, ISBN: 978–1-84816–784–1.

[45] C. Sansour, (1995) A theory and finite element formulation of shells at finite deformations including thickness change: circumventing the use of a rotation tensor. Archives of Applied Mechanics, 10:194–216.

[46] S. Hartmann, S. Brunssen, E. Ramm, B. Wohlmuth (2007) Unilateral non-linear dynamic contact of thin-walled structures using a primal-dual active set energy. International Journal for Numerical Methods in Engineering. 70:883–912.

[47] S. Klinkel, W. Wagner (1997) A geometrical nonlinear brick element based on the EAS method. International Journal for Numerical Methods in Engineering, 40:4529–4545.

[48] R.J.A. Alves de Sousa, R.P.R. Cardoso, R.A. Fontes Valente, J.W. Yoon, J.J. Grácio, R.M. Natal Jorge (2005) A new one–point quadrature enhanced assumed strain (EAS) solid–shell element with multiple integration points along thickness: Part I – geometrically linear applications. International Journal for Numerical Methods in Engineering, 62(7):952–977.

[49] C. Miehe (1998) A theoretical and computational model for isotropic elastoplastic stress analysis in shells at large strains. Computer Methods in Applied Mechanics and Engineering, 155:193–233.

[50] J.C. Simo, S. Rifai (1990) A class of mixed assumed strain methods and the method of incompatible modes. International Journal for Numerical Methods in Engineering, 29:1595–1638.

[51] R.A. Arciniega, J.N. Reddy (2007) Large deformation analysis of functionally graded shells, International Journal of Solids and Structures, 44:2036–2052.

[52] J. Reinoso, M. Paggi, R. Rolfes (2016) A computational framework for the interplay between delamination and wrinkling in functionally graded thermal barrier coatings, Computational Materials Science 116:82–95.

[53] B.D. Coleman, W. Noll (1963) The thermodynamics of elastic materials with heat conduction and viscosity. Archive for Rational Mechanics and Analysis. 13:167–178.

[54] Bischoff, M., Wall, W.A., Bletzinger, K.–U., Ramm, E. (2004) Chapter 3: Models and Finite Elements for Thin–Walled Structures, in: (E. Stein, R. de Borst, T.J.R. Hughes, eds): Encyclopedia of Computational Mechanics, Volume 2: Solids and Structures, John Wiley & Sons, Ltd.

[55] M. Bischoff (1999) Theorie und Numerik einer dreidimensionalen Schalenformulierung. PhD Dissertation Universität Stuttgart, Germany.

[56] U. Andelfinger, E. Ramm (1993) EAS–Elements for two–dimensional, three–dimensional, plate and shells and their equivalence to HR–elements. International Journal for Numerical Methods in Engineering, 36: 1413 – 1449.

[57] R. Hauptmann, K. Schweizerhof (1998) A systematic development of solid–shell element formulations for linear and non–linear analyses employing only displacement degrees of freedom. International Journal for Numerical Methods in Engineering 42:4969.

[58] K.Y. Sze, X.H. Liu, S.H. Lo (2004) Popular benchmark problems for geometric nonlinear analysis of shells. Finite Elements in Analysis and Design, 40:15511569.

[59] Arciniega, R.A. (2005) On a tensor–based finite element model for the analysis of shell structures. PhD Dissertation, Department of Mechanical Engineering, Texas AM University.

[60] J.C. Simo, D.D. Fox, M.S. Rifai (1990) On a stress resultant geometrically exact shell model. Part III: Computational aspects of the nonlinear theory. Comput Meth Appl Mech Eng 1990;79:21–70.

[61] M. Schwarze, S. Reese (2009) A reduced integration solid–shell finite element based on the EAS and the ANS conceptGeometrically linear problems. International Journal for Numerical Methods in Engineering, 2009; 80:1322-1355.